JOURNAL OF GEOPHYSICAL RESEARCH, VOL. 114, A08307, doi:10.1029/2008JA013966, 2009

Neutral wind control of the Jovian magnetosphere-ionosphere current system

Chihiro Tao,[1] Hitoshi Fujiwara,[1] and Yasumasa Kasaba[1]

Received 5 December 2008; revised 4 May 2009; accepted 8 May 2009; published 25 August 2009.

[1] In order to clarify the role of neutral dynamics in the Jovian magnetosphere-ionosphere-thermosphere coupling system, we have developed a new numerical model that includes the effect of neutral dynamics on the coupling current. The model calculates axisymmetric thermospheric dynamics and ion composition by considering fundamental physical and chemical processes. The ionospheric Pedersen current is obtained from the thermospheric and ionospheric parameters. The model simultaneously solves the torque equations of the magnetospheric plasma due to radial currents flowing at the magnetospheric equator, which enables us to update the electric field projected onto the ionosphere and the field-aligned currents (FACs) depending upon the thermospheric dynamics. The self-consistently calculated temperature and ion velocity are consistent with observations. The estimated neutral wind field captures the zonally averaged characteristics in previous three-dimensional models. The energy extracted from the planetary rotation is mainly used for magnetospheric plasma acceleration below 73.5° latitude while consumed in the upper atmosphere, mainly by Joule heating at above 73.5° latitude. The neutral wind dynamics contributes to a reduction in the electric field of 22% compared with the case of neutral rigid corotation. About 90% of this reduction is attributable to neutral winds below the 550-km altitude in the auroral region. The calculated radial current in the equatorial magnetosphere is smaller than observations. This indicates that the enhancement of the background conductance and/or the additional radial current at the outer boundary would be expected to reproduce the observed current.

Citation: Tao, C., H. Fujiwara, and Y. Kasaba (2009), Neutral wind control of the Jovian magnetosphere-ionosphere current system, *J. Geophys. Res.*, *114*, A08307, doi:10.1029/2008JA013966.

1. Introduction

[2] Jupiter is the largest planet in the solar system, whose dominant energy source for the magnetosphere is its fast planetary rotation. The energy is transported from the near-rigidly corotating neutral atmosphere to the magnetosphere through ion-neutral collisions in the ionosphere. On the other hand, the dynamics in the thermosphere-ionosphere region is largely affected by the ion drag and Joule heating due to the electric field that originates from the lag of out-flowing magnetospheric plasma. Therefore the dynamics in the Jovian thermosphere, ionosphere, and magnetosphere are strongly related to each other.

[3] Jovian magnetosphere-ionosphere coupling processes have been widely studied using magnetosphere-ionosphere coupling current models. The models were developed to understand the magnetospheric plasma motion driven by the Jovian atmosphere through electromagnetic coupling [e.g., *Hill*, 1979]. The coupling processes are summarized as follows. Assuming conservation of angular momentum, a parcel of plasma which is initially in near-corotation with the planet will develop a lag in angular velocity behind corotation as it is transported radially outward from the Io torus. In the reference frame which corotates with the planet, an electric field is induced at high latitudes in the ionosphere. This electric field is equatorially directed. The Pedersen current in the model flows in the same direction. As a result of current closure in the steady state, downward and upward field-aligned currents (FACs) are established as we move from higher (subcorotating magnetosphere) to lower ionospheric latitudes (corotating magnetosphere). The upward FAC is principally carried by downward-precipitating electrons. This region corresponds to the main auroral oval. In the magnetospheric equatorial plane, the radially outward current accelerates the lagging plasma toward corotation through the $\vec{J} \times \vec{B}$ force. The observed angular velocity of the plasma is higher than the velocity which would be in the absence of the associated transfer of torque from the ionosphere [e.g., *McNutt et al.*, 1981].

[4] *Hill* [1979] derived the steady state angular velocity profile of the out-flowing magnetospheric plasma by solving the equation of motion assuming a dipole magnetic field and a fixed ionospheric Pedersen conductivity. In the

[1]Department of Geophysics, Tohoku University, Aoba-ku, Sendai, Miyagi, Japan.

0148-0227/09/2008JA013966$09.00

planetary corotating frame, ionospheric ions drift in the antirotational direction under the combined action of the planetary magnetic field and the ionospheric electric field. The neutral atmosphere is also accelerated in the same antirotation direction through ion-neutral collisions. *Huang and Hill* [1989] introduced a realistic neutral delay relative to the planetary rotation that acts to reduce the Pedersen current. In fact, an ion wind with a velocity of 0–3 km/s was obtained from observations of the Doppler shift of H_3^+ infrared emissions [*Rego et al.*, 1999; *Stallard et al.*, 2003]. Several theoretical approaches have been used to obtain the FAC distribution associated with the main auroral oval [e.g., *Hill*, 2001; *Cowley and Bunce*, 2001], to clarify its dependence on the magnetospheric magnetic field [e.g., *Pontius*, 1997; *Cowley et al.*, 2002], and to investigate the responses of the coupling system to solar wind variations [e.g., *Cowley and Bunce*, 2003; *Cowley et al.*, 2007]. Including the effects of auroral precipitation on the ionospheric conductance and the FAC, *Nichols and Cowley* [2004] reproduced a narrow auroral oval $\sim 0.6^\circ$ in width, which is in agreement with observations.

[5] The total power input from the magnetosphere to the polar region estimated from the auroral emission, 10^{13}–10^{14} W [*Clarke et al.*, 2004], is much larger than that due to solar EUV radiation, $\sim 10^{12}$ W (estimated from *Schunk and Nagy* [2000]). Ionosphere-thermosphere models have been developed to understand the observed profiles of electron density and temperature and to investigate global ionosphere-thermosphere dynamics driven by energy and momentum inputs in the polar region. Simulations with the Jupiter Thermospheric General Circulation Model (JTGCM [*Bougher et al.*, 2005; *Majeed et al.*, 2005]) suggested that the mechanism for maintaining the high temperature of $\sim$900 K in the equatorial thermosphere observed by the Galileo probe [*Seiff et al.*, 1997] is due to dynamical heating induced by the low-latitude convergence of thermospheric winds originating at higher latitude. *Millward et al.* [2005] investigated the velocity profiles of the neutral wind and plasma with the Jovian Ionospheric Model (JIM [*Achilleos et al.*, 1998]). They showed that the effect of the neutral wind on the coupling system depends upon the polar ionospheric electric field and precipitating electron energy flux through the corresponding direct heating of the neutral atmosphere and an increase in ion-neutral collisions.

[6] These previous thermosphere-ionosphere models, however, generally assumed a static magnetospheric component of the electric field and a fixed auroral electron flux, without any feedback effects from thermospheric dynamics. On the other hand, the magnetosphere-ionosphere models of coupling current usually assumed a simplified form for the thermospheric dynamics, such as a linear relation between thermospheric and magnetospheric angular velocities. The interactions between the thermosphere-ionosphere dynamics and the magnetosphere-ionosphere coupling current system remain largely unknown despite the importance of the feedback for understanding the energy transfer process quantitatively.

[7] In order to understand the coupling processes between the magnetosphere, ionosphere, and thermosphere, especially the role of neutral dynamics on the coupling system, we have developed a new numerical model. The model simultaneously calculates the thermospheric dynamics by considering fundamental physical and chemical processes and the magnetospheric plasma motion with a torque equation, enabling us to self-consistently obtain the electric field imposed on the ionosphere (by magnetospheric motions) and the FAC, which depends partly upon the thermospheric dynamics. This model, therefore, is able to deal with the interactions between the Jovian thermosphere-ionosphere and the magnetosphere, which are strongly related to each other by the current system. Details of the model are described in section 2. Section 3 shows the latitudinal distributions of the current and thermospheric parameters obtained from our model. We compare our results with previous studies in section 4, followed by a discussion concerning the effects of neutral dynamics on the coupling system and current distribution. Finally, the results of this study are summarized with conclusions in section 5.

2. Model

[8] This model solves primitive equations to obtain two-dimensional wind and temperature distributions in the meridional plane in the thermosphere-ionosphere region (see section 2.1) assuming axisymmetry. Fundamental physical and chemical processes are included (see sections 2.2–2.6). The model simultaneously solves the torque equation of the magnetospheric plasma to obtain the electric field imposed on the ionosphere (see section 2.7). The empirical magnetic field model used in this study is described in section 2.8. The numerical method and simulation conditions are summarized in section 2.9.

2.1. Governing Equations for the Thermosphere

[9] The model solves the axisymmetric momentum and energy equations in the pressure coordinate system in order to obtain the distributions of the thermospheric wind and temperature. Parameters are assumed independent of longitude φ, so that the zonal derivative d/dφ is taken to be zero. The axisymmetric equations are written as follows:

$$\frac{\partial u_\varphi}{\partial t} = -\frac{u_\theta}{R_J}\frac{\partial u_\varphi}{\partial \theta}\bigg|_p - w\frac{\partial u_\varphi}{\partial p} + F_{\mathrm{vis}\_\varphi} + F_{\mathrm{cor}\_\varphi} + F_{\mathrm{ion}\_\varphi}, \quad (1)$$

$$\frac{\partial u_\theta}{\partial t} = -\frac{u_\theta}{R_J}\frac{\partial u_\theta}{\partial \theta}\bigg|_p - w\frac{\partial u_\theta}{\partial p} - \frac{g}{R_J}\frac{\partial z}{\partial \theta}\bigg|_p + F_{\mathrm{vis}\_\theta} + F_{\mathrm{cor}\_\theta} + F_{\mathrm{ion}\_\theta}, \quad (2)$$

$$\begin{aligned}\frac{\partial (e+h)}{\partial t} = &-\frac{u_\theta}{R_J}\frac{\partial (e+h+gz)}{\partial \theta}\bigg|_p - w\frac{\partial (e+h+gz)}{\partial p} \\ &+ \left(\vec{F}_{\mathrm{vis}} + \vec{F}_{\mathrm{cor}} + \vec{F}_{\mathrm{ion}}\right)\cdot \vec{u} \\ &+ Q_{\mathrm{con}} + Q_{\mathrm{aurora}} + Q_{\mathrm{solarEUV}} + Q_{\mathrm{IRcool}} \\ &+ Q_{\mathrm{wave}} + Q_{\mathrm{Joule}}, \end{aligned} \quad (3)$$

$$\frac{1}{R_J}\frac{\partial u_\theta}{\partial \theta}\bigg|_p + \frac{\partial w}{\partial p} = 0, \quad (4)$$

where R_J is the Jovian radius of 71,500 km; θ is colatitude; u_φ and u_θ are the zonal (positive toward the east) and

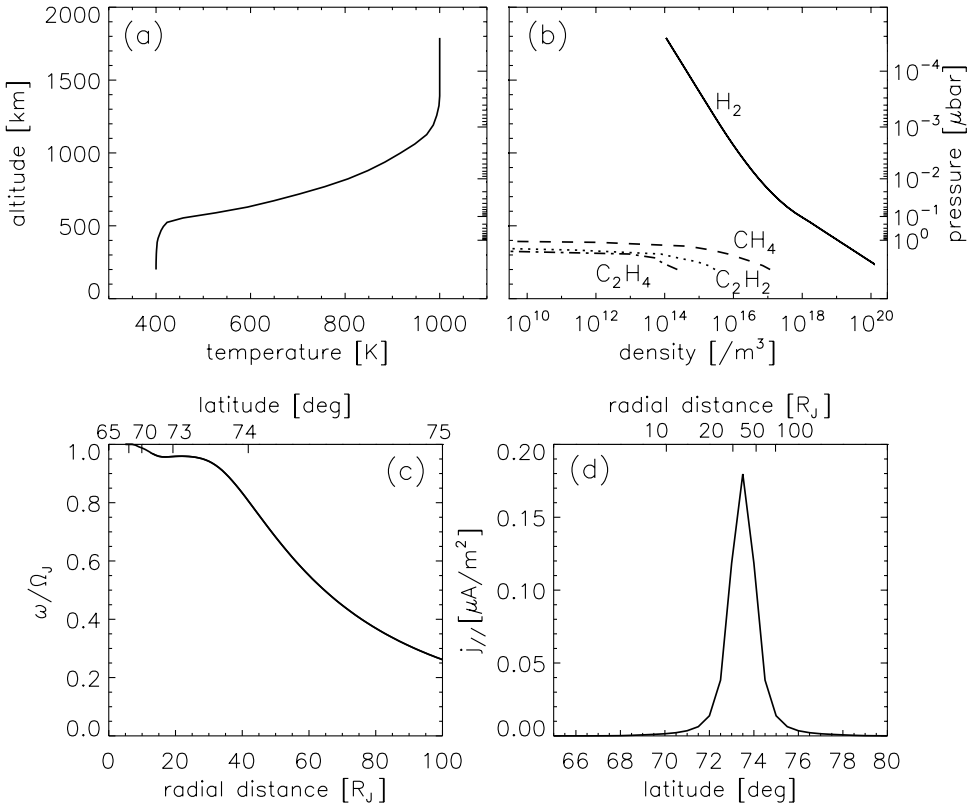

Figure 1. Initial conditions used in this study: vertical profiles of (a) temperature and (b) neutral number densities of H_2 (solid line), CH_4 (dashed line), C_2H_2 (dotted line), and C_2H_4 (dot-dashed line); (c) the radial profile of the angular velocity for the magnetospheric plasma normalized by the planetary angular velocity Ω_J; and (d) the latitudinal distribution of the FAC.

meridional (positive toward the north) neutral wind velocity components, respectively, in the planetary rotation frame of reference; $w \equiv Dp/Dt$ is the convective time derivative of the atmospheric pressure p; z is the height above the 1 bar level; g is the magnitude of gravitational acceleration (25 m/s^2); $e = (1/2)\vec{u} \cdot \vec{u}$ is the specific horizontal kinetic energy; $h = c_p T$ is the enthalpy per unit mass; T is temperature; $c_p = 7k_B/2m_{H_2}$ is the specific heat at constant pressure per unit mass of the H_2 gas; k_B is Boltzmann's constant; and m_{H_2} is the mass of H_2 (3.34×10^{-27} kg). The acceleration terms for the neutral dynamics are the viscosity ($\vec{F}_{vis}$), the Coriolis force and spherical curvature term ($\vec{F}_{cor}$), and the ion-neutral collision force ($\vec{F}_{ion}$). Our model includes the following heating/cooling processes: thermal conduction (Q_{con}), heating by precipitating auroral electrons (Q_{aurora}), solar EUV heating ($Q_{solarEUV}$), cooling by infrared (IR) emission from H_3^+ and hydrocarbons (Q_{IRcool}), wave heating (Q_{wave}), and Joule heating (Q_{Joule}). In addition to equations (1)–(4), the atmospheric number density n is related to pressure and temperature through the gas equation of state

$$p = nk_B T. \tag{5}$$

We refer to the JIM model [*Achilleos et al.*, 1998] for the above equations, the molecular and eddy diffusion coefficients, c_p, and the collision frequency. A pure H_2 atmosphere is considered for the dynamics here because of the dominance of H_2 compared to other species (shown in Figure 1b). There are some differences between JIM and our model in the treatments: the auroral electron precipitation, the effect of solar EUV, ion chemistry, IR cooling, wave heating, the electric field estimation, the magnetic field, and the model region and boundary conditions. These are described in the following sections.

2.2. Auroral Electron Precipitation

[10] The altitude distribution of ionization rate in a H_2 atmosphere caused by electron precipitation is obtained using a parameterized equation (see Appendix A1 [*Hiraki and Tao*, 2008]). A simple and useful formula is employed to apply to the general circulation model with a H_2-dominant atmosphere and to an arbitrary initial energy spectrum of precipitating electrons in the range of 1–200 keV.

[11] The energy flux of precipitating electrons presented by *Nichols and Cowley* [2004] is applied in this study. The energy flux depends on FAC density. The auroral electron distribution is assumed to be isotropic over the downward-going hemisphere and to be represented as a function of electron velocity v by

$$f(v) = \frac{f_0}{(v/v_0)^{\alpha} + (v/v_0)^{\beta}} \mathrm{s}^3/\mathrm{m}^6, \tag{6}$$

where f_0 is a normalization constant described later; constants α and β represent spectral slopes for $v < v_0$ and

$v > v_0$, respectively. The characteristic velocity v_0 is given by

$$v_0 = \sqrt{\frac{2q\Phi}{m_{ele}}} = \sqrt{\frac{2W_{th}}{m_{ele}}\left(\frac{j_{\|i}}{j_{\|i0}} - 1\right)}, \quad (7)$$

where q is the charge; Φ is the field-aligned voltage; m_{ele} is the mass of electrons; $W_{th} = 2.5$ keV is a thermal energy of the magnetospheric electrons; $j_{\|i}$ is the FAC density in the ionosphere; and $j_{\|i0} = 0.0134$ μA/m^2 is the current density it would be without the electrons' acceleration. The total electron flux is scaled to the value $j_{\|i}/q$, where $j_{\|i}$ is calculated in the model (see section 2.7), setting the factor f_0 as follows

$$f_0 = \frac{j_{\|i}}{\pi q}\Big/\int_0^\infty \frac{v^3}{(v/v_0)^\alpha + (v/v_0)^\beta}dv. \quad (8)$$

We apply the case with $\alpha = 2$ and $\beta = 8$ in this study as by *Nichols and Cowley* [2004].

[12] We multiply the ionization rate per unit volume (/m^3/s) by the ionization potential of ~0.03 keV [*Hiraki and Tao*, 2008] and a heating efficiency of 0.3 [*Waite et al.*, 1983; *Achilleos et al.*, 1998], to estimate the heating rate of the neutral gas (J/m^3).

2.3. Solar EUV

[13] The neutral heating rate per unit mass due to the solar EUV radiation $Q_{solarEUV}$ is given by

$$Q_{solarEUV} = \frac{1}{mn}f_s\int_\lambda \frac{d\Phi}{dz}d\lambda = \frac{1}{mn}f_s n\int_\lambda \sigma_a\Phi_0\exp(-\tau)d\lambda, \quad (9)$$

where Φ is the intensity of the solar photon flux; Φ_0 is the unattenuated flux at the top of the atmosphere; σ_a are absorption cross sections [*Schunk and Nagy*, 2000]; f_s is the neutral heating efficiency of 0.5 [*Achilleos et al.*, 1998]; n is the number density; m is the molecular mass; and τ is the optical depth given as $\sum_s \sigma_{as} n_s H_s$ sec χ, where H_s is the scale height of the s-th species and χ is the solar zenith angle. The effects of the planetary curvature on the radiation transmission are included by modifying the optical depth with approximation formulae summarized by *Shimazaki* [1985]. As for Φ_0, we use the EUVAC model [*Richards et al.*, 1994], which is based on the reference spectra derived from sounding rocket observations. This model spectrum provides the solar EUV flux with wavelengths λ of 5–105 nm as a function of the F10.7 index and its 80-day average. We assume the low solar activity conditions (F10.7 = 80 × 10^{-22} W/m^{2}Hz) in this study. Because this model gives the solar flux at the Earth, namely, at a distance of 1 AU from the Sun, the flux value is divided by a factor 5.2^2 for the case of Jupiter (Jupiter is located at 5.2 AU from the Sun). The ionization rates for H_2^+, CH_4^+, and $C_2H_2^+$ from H_2, CH_4, and C_2H_2 are calculated using the appropriate ionization cross sections [*Schunk and Nagy*, 2000; after *Kim and Fox*, 1994]. These cross sections are also used to evaluate σ_a in equation (9). For simplicity, the solar EUV flux is fixed at the daily averaged value depending on latitude.

Table 1. Ion-Neutral Reactions and Rates Used in This Study[a]

Reactions		Rates	References
$H_2 + e^{-*}$	$\rightarrow H_2^+ + e^- + e^{-*}$		1
$H_2 + h\nu$	$\rightarrow H_2^+ + e^-$		2
$CH_4 + h\nu$	$\rightarrow H_2^+ + e^-$ +products		2
$CH_4 + h\nu$	$\rightarrow CH_3^+ + e^-$ +products		3
$CH_4 + h\nu$	$\rightarrow CH_4^+ + e^-$		3
$C_2H_2 + h\nu$	$\rightarrow C_2H_2^+ + e^-$		3
$H_2^+ + H_2$	$\rightarrow H_3^+ + H$	2×10^{-9}	4
$H_3^+ + CH_4$	$\rightarrow CH_5^+ + H_2$	2.4×10^{-9}	4
$CH_3^+ + CH_4$	$\rightarrow C_2H_5^+ + H_2$	1.20×10^{-9}	3
$CH_4^+ + H_2$	$\rightarrow CH_5^+ + H$	3×10^{-11}	4
$CH_5^+ + C_2H_2$	$\rightarrow C_2H_3^+ + CH_4$	1.56×10^{-9}	3
$C_2H_2^+ + H_2$	$\rightarrow C_2H_3^+ + H$	1.8×10^{-12}	after 4
$C_2H_3^+ + CH_4$	$\rightarrow C_3H_5^+ + H_2$	2.00×10^{-10}	3
$C_2H_3^+ + C_2H_2$	$\rightarrow C_4H_3^+ + H_2$	2.16×10^{-10}	3
$C_2H_3^+ + C_2H_4$	$\rightarrow C_2H_5^+ + C_2H_2$	9.30×10^{-10}	3
$C_2H_5^+ + C_2H_2$	$\rightarrow C_3H_3^+ + CH_4$	6.84×10^{-11}	3
	$\rightarrow C_4H_5^+ + H_2$	1.22×10^{-10}	3
$H_3^+ + e^-$	$\rightarrow$ products	$1.15 \times 10^{-7}\ (300/T_e)^{0.65}$	4
$CH_3^+ + e^-$	$\rightarrow$ products	$3.5 \times 10^{-7}\ (300/T_e)^{0.5}$	3
$CH_4^+ + e^-$	$\rightarrow$ products	$3.5 \times 10^{-7}\ (300/T_e)^{0.5}$	3
$CH_5^+ + e^-$	$\rightarrow$ products	$2.78 \times 10^{-7}\ (300/T_e)^{0.52}$	4
$C_2H_2^+ + e^-$	$\rightarrow$ products	$2.71 \times 10^{-7}\ (300/T_e)^{0.5}$	4
$C_2H_3^+ + e^-$	$\rightarrow$ products	$4.6 \times 10^{-7}\ (300/T_e)^{0.5}$	4
$C_2H_5^+ + e^-$	$\rightarrow$ products	$7.4 \times 10^{-7}\ (300/T_e)^{0.5}$	3
$C_3H_n^+ + e^-$	$\rightarrow$ products	$7.5 \times 10^{-7}\ (300/T_e)^{0.5}$	4
$C_4H_n^+ + e^-$	$\rightarrow$ products	$7.5 \times 10^{-7}\ (300/T_e)^{0.5}$	4

[a]References: 1, *Hiraki and Tao* [2008] (section 2.2 and Appendix A); 2, *Schunk and Nagy* [2000]; 3, *Kim and Fox* [1994]; 4, *Perry et al.* [1999]. T_e denotes the electron temperature. Unit of measurement for the rate is cm^3/s.

2.4. Ion Chemistry and Conductivity

[14] Considering a simplified set of neutral-ion chemical reactions (see Table 1) for nine ions (H_2^+, H_3^+, CH_4^+, CH_5^+, $C_2H_2^+$, $C_2H_3^+$, $C_2H_5^+$, $C_3H_n^+$, and $C_4H_n^+$, where the latter two ions represent classes of ions) and four fixed neutral spaces (H_2, CH_4, C_2H_2, and C_2H_4; see section 2.9 and Figure 1), our model solves ion composition equations using the implicit method. The major production and loss reactions are selected from the detailed ion chemical model presented by *Kim and Fox* [1994] to describe the fundamental ionospheric structure and conductance. For simplicity, we do not take into account either transport by winds or diffusion of chemical species.

[15] The collision frequencies of ions ν_{ion_n} and electrons ν_{ele_n} with H_2 are taken from the studies of *Chapman and Cowling* [1970] and *Danby et al.* [1996]. Using the parallel conductivity for ions $\sigma_{ion} \equiv (n_{ion}q_{ion}^2)/(m_{ion}\nu_{ion\_n})$ and electrons $\sigma_{ele} \equiv (n_{ele}q_{ele}^2)/(m_{ele}\nu_{ele\_n})$, we derive the Pedersen conductivity from $\sigma_P = \nu_{ion\_n}^2\,\sigma_{ion}/(\nu_{ion\_n}^2 + \Omega_{c\ ion}^2) + \nu_{ele\_n}^2\,\sigma_{ele}/(\nu_{ele\_n}^2 + \Omega_{c\ ele}^2)$, where n is the density; q is the charge; m is the mass of ions or electrons; Ω_c is the cyclotron frequency; and subscripts "ion", "ele", and "n" indicate parameters related to ions, electrons, and neutrals, respectively. The ionospheric Pedersen conductance Σ is obtained by integrating the conductivity with the altitude.

2.5. IR Cooling

[16] The IR cooling rate due to the H_3^+ and hydrocarbon emissions shown in the JTGCM calculation at the equator [*Bougher et al.*, 2005] is adopted for this study. The applied cooling rate varies as a function of the H_3^+ number density,

Table 2. Main Characteristics of the Six Sonic Waves and Their Heating Rates Based on the Study of *Schubert et al.* [2003]

Period (min)	Horizontal Wavelength (km)	Maximum Heating	
		Rates (W/m^3)	Altitude (km)
1	132	3.5×10^{-9}	750
1	200	1.0×10^{-11}	1200
3	(vertical propagation)	6.0×10^{-12}	1600
5	510	8.0×10^{-9}	600
5	660	4.5×10^{-12}	1200
5	1000	5.0×10^{-12}	1700

$[H_3^+]$, and temperature, T, calculated by our model, as follows,

$$Q_{\mathrm{IRcool}} = Q_{\mathrm{IRcool\_JTGCM}} \times \frac{\left[H_3^+\right]}{\left[H_3^+\right]_{\mathrm{JTGCM}}} \exp\left(-\frac{1}{T} + \frac{1}{T_{\mathrm{JTGCM}}}\right), \tag{10}$$

where T_{JTGCM} and $[H_3^+]_{\mathrm{JTGCM}}$ are the temperature and H_3^+ number density, respectively, obtained from the JTGCM. Since Figure 15 in the study of *Bougher et al.* [2005] contains scaling errors on the x axis as pointed by *Melin et al.* [2006], we apply their cooling rate $Q_{\mathrm{IRcool\_JTGCM}}$ divided by 1000 in this study.

2.6. Wave Heating

[17] Long time integration of our model simulation shows that middle- or low-latitude heat sources are necessary to maintain the observed high temperature of ~900 K. There are three candidates for the heating process. One is the heavy ion precipitation at low latitudes corresponding to X-ray emissions found by the ROSAT X-ray observations [*Waite et al.*, 1997]. Another is heating due to the dissipation of gravity waves propagating from the lower altitude region [*Young et al.*, 1997]. A wavy temperature profile, which is probably a manifestation of gravity waves, was observed by the Galileo entry probe [*Seiff et al.*, 1997]. The third candidate is heating by sonic waves originating from lightning [*Schubert et al.*, 2003]. In this model we apply heating due to sonic waves for two reasons. Firstly, the effect of the heavy ion precipitation was estimated to be small from the JTGCM simulation [*Bougher et al.*, 2005]. Secondly, according to *Matcheva and Strobel* [1999], a realistic treatment of gravity waves would actually have cooling effects on the thermosphere. *Schubert et al.* [2003] considered six types of sonic waves (Table 2) with periods of one (horizontal wavelengths of 132 and 200 km), three (vertical propagation), and five minutes (horizontal wavelengths of 510, 660, and 1000 km). The altitude profiles of their estimated heating rates are applied in our model. These waves have maximum heating rates of 3.5×10^{-9}, 1×10^{-11}, 6×10^{-12}, 8×10^{-9}, 4.5×10^{-12}, and 5×10^{-12} W/m^3 at altitudes of 750, 1200, 1600, 600, 1200, and 1700 km, respectively. These heating rates are assumed to be uniform at all latitudes.

2.7. Current and Magnetospheric Plasma Convection

[18] The magnetospheric plasma convection, electric field, and FAC are estimated based on methods used in the magnetosphere-ionosphere coupling models of *Nichols and Cowley* [2004] as follows. The ionospheric Pedersen current J_{i} per unit azimuthal length is obtained using the conductivity σ_{P} as follows:

$$J_{\mathrm{i}} = \int_z \sigma_{\mathrm{P}} E_{\mathrm{n}} \mathrm{d}z = \int_z \sigma_{\mathrm{P}} B_{\mathrm{i}} (u_{\mathrm{n}} - r_{\mathrm{i}} \omega) \mathrm{d}z, \tag{11}$$

where E_{n} is the electric field in the rest frame of the neutral atmosphere; B is the magnetic field strength; u_{n} is the neutral wind azimuthal velocity in the inertial frame ($\equiv r_{\mathrm{i}} \Omega_{\mathrm{J}} - u_{\varphi}$); r is the distance from the rotation axis; Ω_{J} is the planetary angular velocity equal to 1.76×10^{-4} rad/s; and ω is the angular velocity of the magnetospheric plasma. Subscripts "i" and "e" (seen below) indicate parameters in the ionosphere and at the magnetospheric equator, respectively. From current conservation, the FAC $j_{\parallel}$ and radial current per unit azimuthal length at the magnetospheric equator J_{e} are obtained from

$$j_{\parallel \mathrm{i}} = -\frac{1}{r_{\mathrm{i}}} \frac{\partial J_{\mathrm{i}}}{\partial \theta_{\mathrm{i}}}, \tag{12}$$

$$j_{\parallel \mathrm{e}} / B_{\mathrm{e}} = j_{\parallel \mathrm{i}} / B_{\mathrm{i}}, \tag{13}$$

$$J_{\mathrm{e}} = 2 \int_{2R_{\mathrm{J}}}^{r_{\mathrm{e}}} j_{\parallel \mathrm{e}} \, \mathrm{d}r_{\mathrm{e}}. \tag{14}$$

The factor two in equation (14) is based on the assumption of north-south symmetry, i.e., the magnetospheric equator connects to both the northern and southern high-latitude regions. The electron flux at the next time step of the calculation is obtained by equations (6)–(8) using $j_{\parallel \mathrm{i}}$ as mentioned above.

[19] For the magnetospheric plasma, assuming that the plasma density is independent of local time (azimuthal symmetry) and time, we obtain the following relation from the equation of continuity,

$$\frac{\partial (\rho \vec{\mathbf{v}})}{\partial r_{\mathrm{e}}} = 0 \quad \therefore M_{\mathrm{flux}} \equiv 2\pi \rho D v_{\mathrm{r}} r_{\mathrm{e}} = \mathrm{const.}, \tag{15}$$

where ρ is the magnetospheric plasma density; $\vec{\mathbf{v}}$ is the plasma velocity whose radial component is v_{r}; and D is the thickness of the plasma sheet assumed to be ~2 R_{J}. The outward plasma mass flux is taken to be $M_{\mathrm{flux}} \sim 1000$ kg/s [e.g., *Hill*, 1980]. The outward-flowing plasma is subject to an azimuthal torque due to the $\vec{\boldsymbol{J}} \times \vec{\boldsymbol{B}}$ force associated with a radial current at the magnetospheric equator. The equation of motion in the azimuthal direction for the axisymmetric system is written as follows,

$$2\pi \rho D r_{\mathrm{e}}^3 \frac{\partial \omega}{\partial t} + M_{\mathrm{flux}} \frac{\partial \left(r_{\mathrm{e}}^2 \omega\right)}{\partial r} = 2\pi r_{\mathrm{e}}^2 J_{\mathrm{e}} |B_{\mathrm{ze}}|, \tag{16}$$

where B_{ze} is the north-south component of the magnetic field at the magnetospheric equator.

[20] The radial distribution of the plasma density in the magnetospheric equator is set as

$$n_e(r_e) = 1.73 \times 10^3 (r_e/R_J)^{-2.75}\ \mathrm{cm}^{-3}, \quad (17)$$

based on observations by Voyager 1 [*Barbosa et al.*, 1979]. Since the Jovian magnetospheric plasma is mainly composed of oxygen ions, sulfur ions, and protons, we set the mean ion mass as 20 amu [*Thomas et al.*, 2004].

2.8. Magnetic Field Model and Magnetosphere-Ionosphere Mapping

[21] A spin-aligned dipole magnetic field is assumed for the ionosphere with a strength of $B_{J0} = 4.35 \times 10^{-4}$ T at the equator on the planetary surface, 1 R_J. A flux function F is related to the field components by $\vec{\mathbf{B}} = 1/r\vec{\nabla}F \times \hat{\varphi}$, where $\hat{\varphi}$ is the unit vector in the azimuthal direction. If the magnetic field at high latitudes is regarded as uniform in the ionosphere with a constant value of $2B_{J0}$, the flux function in the ionosphere is represented as a function of colatitude θ_i,

$$F_i(\theta_i) = 2B_{J0}r_i^2 = 2B_{J0}R_J^2(\sin\theta_i)^2. \quad (18)$$

The flux function described by equation (18) includes an error of less than 3% in the 65°–85° latitude region because of the choice of the uniform magnetic field strength. The magnetic field and flux function at the magnetospheric equator are given by an empirical model used by *Nichols and Cowley* [2004]:

$$B_{ze}(r_e) = -\left\{3.335 \times 10^5 \left(\frac{R_J}{r_e}\right)^3 \exp\left(-\frac{r_e}{14.501R_J}\right)^{\frac{5}{2}} + 5.4 \times 10^4 \left(\frac{R_J}{r_e}\right)^{2.71}\right\}\ [\mathrm{nT}], \quad (19)$$

$$F_e(r_e) = 2.841 \times 10^4 + 9.199 \times 10^3 \Gamma\left(-\frac{2}{5}, \left(\frac{r_e}{14.501R_J}\right)^{5/2}\right) + \frac{5.4 \times 10^4}{2.71 - 2}\left(\frac{R_J}{r_e}\right)^{2.71-2}\ \left[\mathrm{nT}\,R_J^2\right], \quad (20)$$

where Γ is the incomplete gamma function $\Gamma(a,z) = \int_z^\infty t^{a-1}e^{-t}\,dt$. The expression F = constant defines a shell of the magnetic field lines which cross the magnetic equator at the same radial distance. Magnetic mapping between the magnetospheric equatorial plane and the ionosphere is defined by the equality $F_i = F_e$. Use of this equality with equations (18) and (20) allows us to map radial distance in the magnetospheric equatorial plane to the magnetically conjugate ionospheric colatitude θ_i.

2.9. Numerical Methods and Simulation Condition

[22] The primitive equations shown in section 2.1 are solved in the pressure coordinate system with the finite difference method. The first-order upwind difference with the modified Euler time-integral method [*Durran*, 1999] is used for the numerical calculations. The horizontal latitudinal resolution is 0.5° with 181 points between the equator and the pole. This resolution is chosen to satisfy the following conditions: the width of the auroral oval (full width of a few degrees) can be resolved, and the spatial resolution affects the energy transfer rate from the magnetosphere to the atmosphere by less than 10% compared with that obtained in runs with 10 times as high resolution. The vertical resolution is 0.4 scale heights (33–166 km for the corresponding region) with 35 layers from 10 μbar (=200 km altitude, following *Grodent et al.* [2001]) to 0.01 nbar (~1570 km), applying the staggered grid method (type C' in the study of *Tokioka* [1978]). This method distributes variables over the vertical grids to treat internal waves without computational modes. Auroral electrons precipitate into this altitude region. The solar EUV radiation is also absorbed completely within the region. At the lower boundary the wind velocity is set to 0 m/s, i.e., rigid corotation, while the temperature is set to 400 K. The velocity and temperature at the upper boundary take the same values as those at the adjacent pressure level. In order to avoid numerical oscillations, we apply a numerical low-pass filter (3-point weighted running mean) in the latitude and altitude distributions for u_φ, u_θ, and temperature T.

[23] As for the magnetospheric part of our model, the momentum equation (16) is solved with the upwind difference scheme in the equatorial radial range 2–97 R_J with a resolution of 1 R_J. The magnetospheric plasma is assumed to be corotating at the inner boundary, so that $\omega/\Omega_J = 1$. Io rotates at ~6 R_J, while we choose the inner boundary at 2 R_J in order to reduce the effect of the inner boundary on the auroral region of main interest here. The effect of the discontinuity of the magnetospheric plasma at Io's orbit is beyond the scope of this study. Since the ionospheric region at latitudes above 76° corresponds to a radial distance greater than 97 R_J in the magnetospheric equator, we assume the magnetospheric convection mapped to high latitudes above 76° has a constant corotation angular velocity equal to 0.099 Ω_J at 97 R_J (this is the calculated value, see section 3.1). Previous polar cap models [e.g., *Cowley et al.*, 2005] assumed an angular velocity profile based on observations with ~0.25 Ω_J in the outer magnetosphere region (~76°–80°) for their "low" velocity case and ~0.091 Ω_J in the open field region (~80°–90°) based on previous observations. Since the constant corotation angular velocity in our model, 0.099 Ω_J, is almost the same as that in the open field region presented by *Cowley et al.* [2005], our simplified treatment of the polar thermosphere may not be too unrealistic. Although the open-closed field boundary would provide a shear in plasma angular velocity and FACs as discussed by *Cowley et al.* [2005], our model does not include the effects of the open-closed field boundary in this study. We focus our attention on the large-scale dynamics, while local structures, e.g., the open-closed field boundary, are beyond the scope of this study.

[24] The initial profiles of the thermospheric temperature, neutral density, pressure, and mixing ratios of CH_4, C_2H_2, and C_2H_4 are based on observations referred to by *Perry et al.* [1999]. Figure 1 shows the initial profiles of neutral density, thermospheric temperature, FAC, and magnetospheric plasma velocity. In order to achieve efficient calculations, we perform simulations separately for (1) the thermospheric dynamics and temperature, and the (2) magnetospheric plasma dynamics, both with a time resolution of

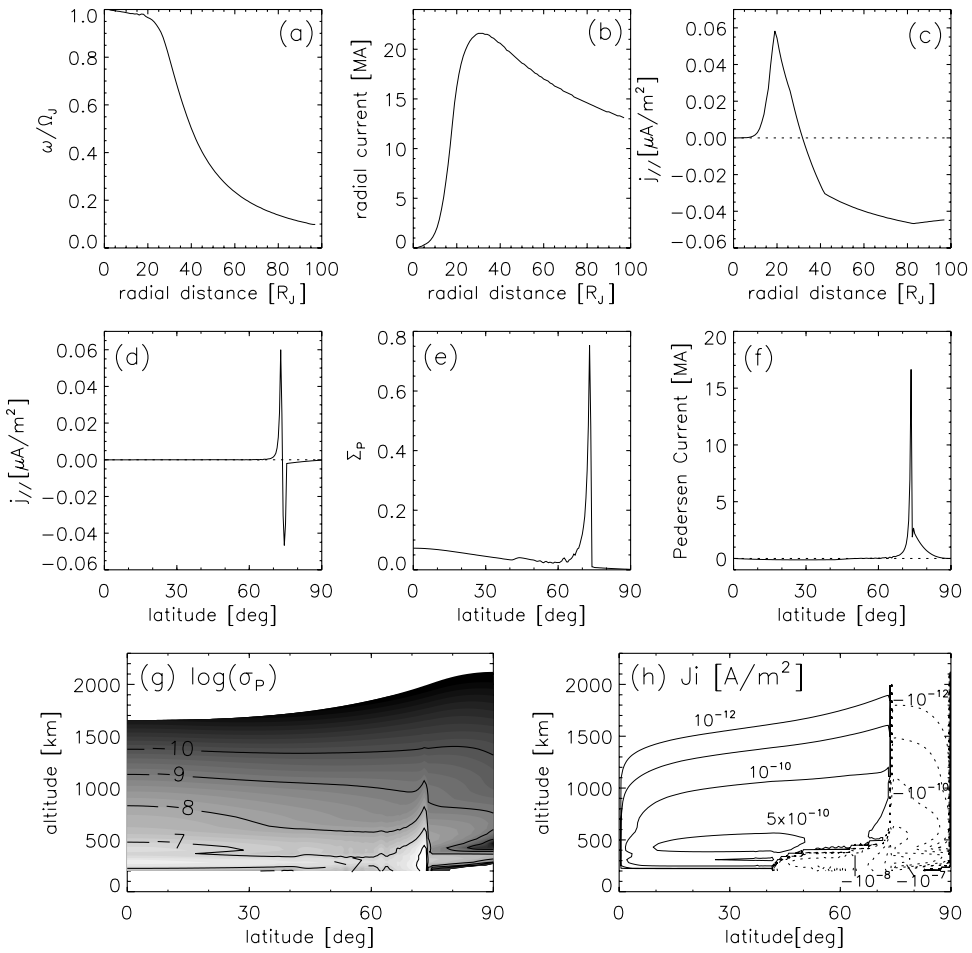

Figure 2. The current parameters calculated in the model showing the radial profiles of (a) the normalized angular velocity of the magnetospheric plasma, (b) the azimuthally integrated radial current at the magnetospheric equator, and (c) the FAC density at the feet of the magnetic field lines in the ionosphere, together with the ionospheric latitude distributions of (d) the FAC density, (e) the Pedersen conductance, and (f) the height-integrated and azimuthally integrated Pedersen current. Contour maps of (g) the Pedersen conductivity (mho/m) and (h) the Pedersen current density (A/m^2) as a function of latitude and altitude. In Figure 2h, the contour lines denoted by solid and dotted lines indicate positive (poleward) and negative (equatorward) currents, respectively.

30 s. The parameters calculated in both (1) and (2) are transferred to the other part of the calculation every 0.5 planetary rotations, during a 10-min interval. During this transfer time, we solve (1) and (2) with a time resolution of 10 s.

3. Results

[25] The newly developed model described in the previous sections provides a quasisteady state after a time integration of 200 rotation periods (~83 Earth-days). The results at 200 rotations are shown hereafter.

3.1. Magnetospheric Parameters and Current Distribution

[26] Figure 2 shows the distributions of the plasma angular velocity, radial current, and FAC versus radial distance at the magnetospheric equator, and the FAC, ionospheric Pedersen conductance, height-integrated current, conductivity, and current density versus latitude in the ionosphere. The plasma angular velocity ω is normalized to the planetary angular velocity Ω_J as shown in Figure 2a. The plasma angular velocity has larger values than those expected from angular momentum conservation because of the acceleration due to the coupling current system. Our results show that the plasma angular velocity drops to 50% of the planetary angular velocity at 40 R_J, and is 9.9% at 97 R_J. For comparison, the plasma angular velocity would fall to 2.1% and 0.37% respectively at 40 and 97 R_J in the case of the angular momentum conservation without the current system. The azimuthally integrated radial current increases with radius for radial distances less than 30 R_J and has a maximum value of 21.6 MA at 31 R_J, and then decreases gradually (Figure 2b). We show the FAC density in the ionosphere at the feet of the field lines versus radial distance in the magnetospheric equator and versus latitude in Figures 2c and 2d, respectively. The FAC density has a maximum value of 0.059 μA/m^2 at 19 R_J and 73° latitude. A positive sign for the FAC means a current flowing from the ionosphere to the magnetosphere. The FAC flows from

the ionosphere to the magnetosphere within radial distances of 31 R_J and latitudes of 73°, and flows from the magnetosphere to the ionosphere outside these regions. The latitude distribution of the integrated Pedersen conductance (Figure 2e) has a similar profile to the FAC in the region to 74° latitude, where electrons precipitate into the atmosphere. The ionospheric conductance has a maximum value of 0.75 mho at 73° latitude. In the region outside 60°–75° latitude, where very little or no electrons precipitate, the conductance is mainly caused by solar EUV. The conductance takes a local maximum value of 0.073 mho at the equator because of the small solar zenith angle. Figure 2f shows the height-integrated Pedersen current. It has a maximum value of 16.6 MA at 73.5° latitude. The altitude and latitude distribution of the ionospheric Pedersen conductivity is shown in Figure 2g using a logarithmic scale. The maximum value of 3.9×10^{-6} mho/m appears at 73° latitude and 254 km altitude. Figure 2h shows the Pedersen current in the ionosphere. The Pedersen current flows equatorward (negative values shown by dashed lines) at high latitudes, while poleward (positive values shown by solid lines) at lower latitudes below 73°. It has a minimum value of -7.2×10^{-7} A/m^2 at 73.5° latitude and 254 km altitude.

3.2. Thermospheric Parameters

[27] Figure 3 shows the height and latitude distribution of the thermospheric temperature, neutral wind velocity, and H_3^+ density. The temperature is highest at high altitudes and latitudes with a maximum value of 1020 K at 1179 km in the polar region (Figure 3a). The value decreases below 1000 km with decreasing latitude. The temperature difference between high latitudes and the equator is ~250 K in the high altitude region (~1000 K at 75°–90° latitudes and ~750 K at the equator), while the difference around 300 km altitude is ~60 K (~480 K at 80°–90° latitudes and 420 K at the equator).

[28] The zonal wind flows in the anticorotating direction in almost all regions (Figure 3b). The wind velocity has a maximum value of 742 m/s at 74.5° at the top of the atmosphere. On the other hand, the wind velocities show small values in the low altitude regions at high latitudes and in the high altitude regions at the equator: ~100 m/s at 74.5° at 544 km and at the equator at 1157 km.

[29] Figure 3c shows the meridional wind distribution, where positive (red) and negative (blue) values mean poleward and equatorward winds, respectively. Equatorward wind is seen above 1500 km at ~70°–90° latitudes and above 400 km in the low latitude region, while poleward meridional winds occur in the other regions. The maximum value of the equatorward wind is 72 m/s at 74° at the top of the atmosphere. In the latitude region above 75°, poleward winds extend up to 1800 km altitude with a maximum velocity of 17 m/s at 79.5° and 1349 km altitude.

[30] The vertical wind distribution is shown in Figure 3d, where positive (red) and negative (blue) values denote upward and downward winds, respectively. The maximum upward wind is seen at 75° at 1251 km with a value of 0.75 m/s. The region of the strongest upward wind is narrow (~75°–80°) below 1200 km, but extends more widely in the polar region above 1400 km. Downward wind is seen below 74° and in the latitude region 80°–90° below 1400 km, with a minimum velocity of −0.78 m/s at 74° at the top of the atmosphere.

[31] Figure 3e shows the H_3^+ distribution. Two major enhanced regions are seen. One is a region where H_3^+ shows broad enhancement above 500 km due to solar EUV ionization, with a local maximum of 9.1×10^9/m^3 at 959 km at the equator. The other enhancement region is a latitudinally confined enhancement around 73° due to auroral electron ionization, with a local maximum of 4.5×10^{10}/m^3 at 419 km.

[32] Two convection cells are seen in Figure 3a. One is a large counterclockwise circulation consisting of upward flows at ~75°, equatorward flows at higher altitudes, downward flows at lower latitudes, and poleward flows at lower altitudes. The other is the small clockwise circulation in the polar region ~75°–90° latitudes consisting of upward flows at ~75°, poleward flows at higher altitudes, downward flows above 80°, and equatorward flows at lower altitudes.

[33] Figure 4 shows the altitude profiles of (a) the main force terms in the zonal momentum equation (equation (1)), (b) the main force terms in the meridional momentum equation (equation (2)), and (c) the heating/cooling terms in the energy equation (equation (3)) in the high latitude region (averaged over the latitude region 65°–80°). Above 1500 km, the Coriolis force (green lines) and viscosity (orange) terms are major components in the antirotational acceleration of the zonal wind. The ion drag (red) is the dominant force below 1500 km, where the ion density is enhanced by auroral electron precipitation (Figure 4a). The force terms for the meridional wind are almost balanced between the geopotential gradient (blue) and the Coriolis force and spherical curvature term (green, Figure 4b). Joule heating (red) is dominant in almost all regions while wave heating (lime green) and horizontal advection (purple) are also dominant around 900 and above 1600 km. The adiabatic expansion of the neutral gas (dark blue) and the heat conduction (green) work effectively as cooling processes (Figure 4c).

4. Discussion

4.1. Validation of Thermosphere-Ionosphere Model

[34] In this section we compare simulation results obtained by our model, JTGCM, and JIM with observations to validate the effectiveness of our model. These models apply different energy inputs into the polar region by auroral electrons and currents. Since their impact on the ionospheric conductance and thermosphere dynamics is large, we first briefly review the auroral energy flux in each model.

[35] JTGCM uses the ionization and heating rates calculated by *Grodent et al.* [2001], which corresponds to a FAC density of 8.7 μA/m^2. Our model calculates the ionization and heating rates caused by auroral electrons using the energy spectrum presented by *Nichols and Cowley* [2004]. The flux is normalized to the FAC density required by the magnetosphere-ionosphere coupling part in our model. The maximum FAC in our model is found to be 0.059 μA/m^2. JIM calculates the effect of monoenergetic electron precipitation for several energy and flux sets. The closest and most comparable case with our FAC density, 0.059 μA/m^2, in

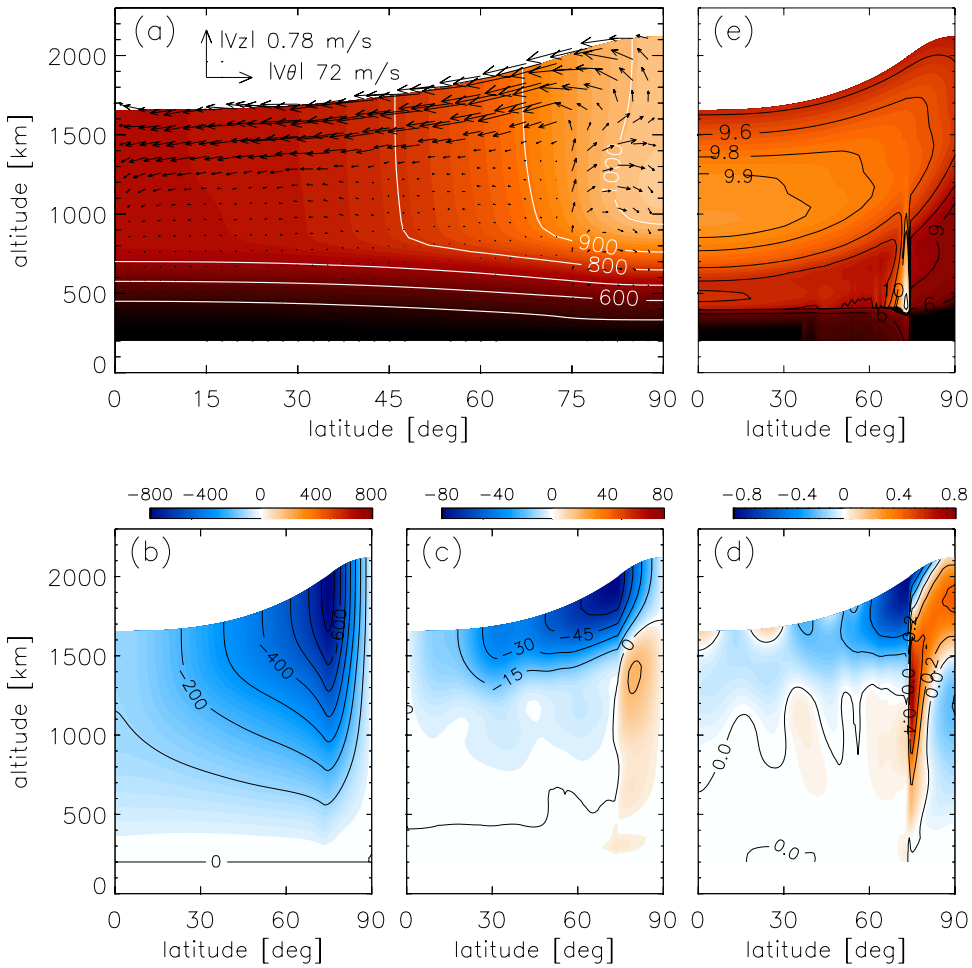

Figure 3. Altitude and latitude distributions of thermosphere-ionosphere parameters calculated in the model showing (a) the temperature (K) and meridional wind field, (b) the zonal wind (m/s), (c) the meridional wind (m/s), (d) the vertical wind (m/s), and (e) the H_3^+ number density (/m^3) using a logarithmic scale. Note that the arrows in Figure 3a are shown using a logarithmic scale with the maximum meridional and vertical components of the neutral wind being 72 and 0.78 m/s, respectively. In Figures 3b–3d, positive (negative) values shown by warm (cool) colors denote eastward (westward), northward (southward), and upward (downward) components, respectively.

JIM settings [*Millward et al.*, 2005] would be the case with the electron flux of 4×10^{11}/m^2. The auroral electron precipitation regions in JIM and JTGCM are based upon observations. They have nonaxisymmetric components of the magnetic and electric fields caused by the inclination of the magnetic axis relative to the rotation axis. Our model does not assume a fixed precipitation region, which is determined self-consistently in the axisymmetric system. Note that the FAC estimated from the observed aurora by *Gustin et al.* [2004a] takes ~0.04–0.4 μA/m^2. Our self-consistently determined FAC is well within and close to the lowest value of the range. Taking into consideration these differences, comparing the auroral parameters in their peak flux regions would be reasonable, and is discussed hereafter.

[36] JTGCM (Case 2 in the study of *Bougher et al.* [2005]), JIM [*Millward et al.*, 2005], and our model calculate the peak H_3^+ density, its altitude, and the height-integrated Pedersen conductivity as ~4×10^{11}/m^3 at 550–700 km (0.1–0.22 μbar) with ~10 mho, ~2×10^{11}/m^3 at 500 km (0.4 μbar) with ~0.25 mho, and 4.5×10^{10}/m^3 at 419 km (0.1 μbar) with 0.75 mho, respectively. The larger conductance from JTGCM than for both JIM and our model is caused by the larger electron flux assumed in JTGCM. The peak density of H_3^+ in JIM is large even taking into account the difference in the input flux. This is affected somewhat by the electron spectrum. The monoenergetic spectrum concentrates and enhances the ionization altitude compared to a multiple Maxwell distribution.

[37] The characteristics of the atmospheric dynamics, i.e., the global atmospheric circulation, obtained in this study are similar to the zonally averaged distribution of wind field calculated by JTGCM [*Bougher et al.*, 2005]. The JTGCM results show the effects of Joule heating and ion drag upon the thermospheric temperature and dynamics. If they used the full values of the Joule heating and ion drag, the calculated temperature and wind became large. They obtained temperatures of 800–850 K, comparable with the observation by the Galileo probe at the equator, when they reduced Joule heating and ion drag to 15% of their full values [*Majeed et al.*, 2005]. *Bougher et al.* [2005] men-

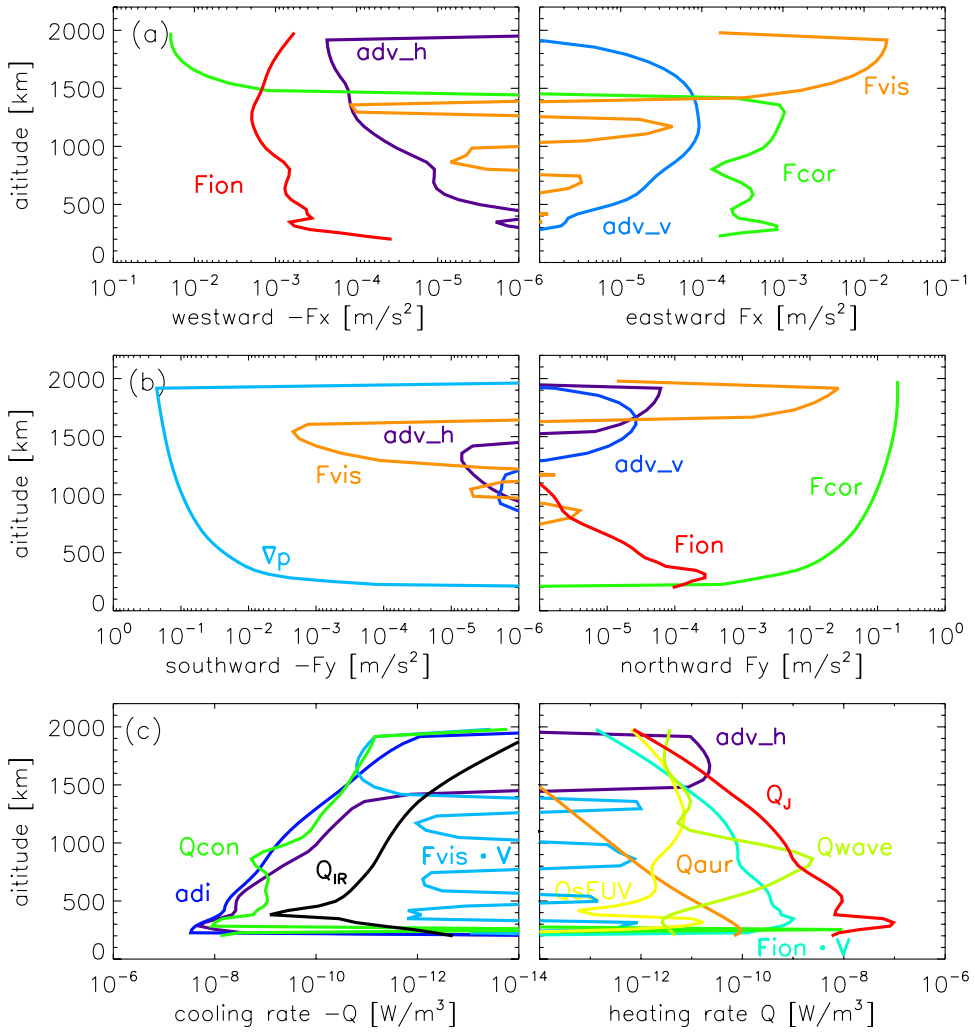

Figure 4. Altitude profiles of (a) the zonal forcing and (b) the meridional forcing terms in the momentum equation and (c) the heating/cooling terms in the energy equation in the auroral region. All the values are averaged over 65°–80°. Positive quantities are shown in the right-hand panel, whereas negative quantities are shown in the left-hand panel. The quantities plotted are as follows: (a) the meridional advection term (labeled as adv_h), the vertical advection term (adv_v), the Coriolis force and spherical curvature term (Fcor), viscosity (Fvis), and ion drag (Fion); (b) the meridional advection term (adv_h), the vertical advection term (adv_v), the geopotential gradient force (∇p), the Coriolis force and spherical curvature term (Fcor), viscosity (Fvis), and ion drag (Fion); and (c) the sum of the meridional and vertical advection terms (adv_h), adiabatic heating/cooling (adi), the work done by viscosity (FvisV), the work done by ion drag (FionV), heat conduction (Qcon), auroral particle heating (Qaur), solar EUV heating (QsEUV), IR cooling (Q_{IR}), wave heating (Qwave), and Joule heating (Q_J).

tioned that the improvements of the electric field and/or ionospheric density estimations are necessary. One possible reason for requiring the reduction ratios for the Joule heating and ion drag would be the lack of feedback processes in association with coupling between the ionospheric conductance, FAC, and the magnetospheric plasma convection.

[38] In our model, we estimate the ion velocity from the balance between the $\vec{J} \times \vec{B}$ force and ion-neutral collisions. The ion velocity takes the maximum absolute value of 2.1 km/s in the planetary rotation frame of reference. This is well within the range of ion velocity (0–3 km/s) observed by the Doppler shift of H_3^+ infrared emissions in the polar region [e.g., *Rego et al.*, 1999]. The temperature values calculated by our model are consistent with those observed in the auroral region [*Grodent et al.*, 2001], i.e., 200–400 K at 200–400 km, 400–850 K at 220–800 km, and 700–1100 K at 350–1300 km. *Lystrup et al.* [2008] obtained altitude profiles for the H_3^+ density and temperature from limb observations of H_3^+ spectra. They showed that the density has a maximum value of $2 \times 10^{11}/m^3$ at 400 km altitude and decreases with increasing altitude to $8 \times 10^9/m^3$ at 1600 km. They found that the exospheric temperature is ~1400 K above 2000 km. The results from our model, an exospheric temperature of ~1150 K and a maximum H_3^+ density of $4.5 \times 10^{10}/m^3$ at 419 km and $4.9 \times 10^9/m^3$ at 1572 km, are consistent with previous observations al-

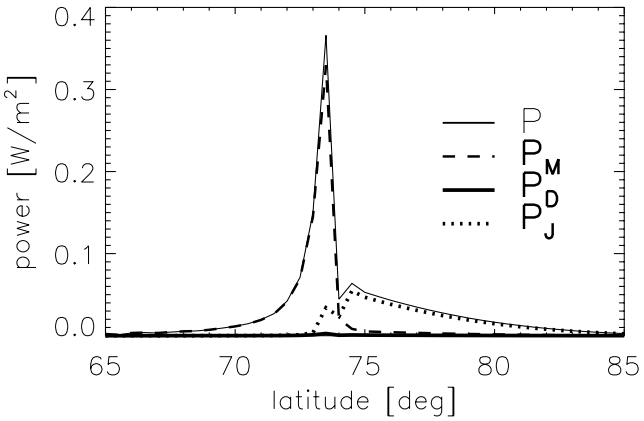

Figure 5. Latitude distributions of the total power per unit area extracted from the planetary rotation P (solid line), the power used for magnetospheric plasma acceleration P_M (bold dashed line), and that consumed in the upper atmosphere as Joule heating P_J (bold dotted line) and ion drag power P_D (bold solid line).

though our results show slightly smaller values than observations.

[39] The differences in ion density and conductance between models are generally understood by different assumptions between models. On the other hand, the thermospheric dynamics obtained in this study is similar to the zonally averaged ones by JTGCM. The thermospheric temperature, ion velocity, and ion density shown in this study are consistent with previous observations, while the calculated values of the ion density in this study are slightly smaller than observations. This would be related to the auroral particle precipitation assumed in our model, which is discussed more in detail in section 4.4. From these comparisons, the effectiveness of our model for calculating the thermospheric and ionospheric parameters is validated. We will discuss the energy transfer in the magnetosphere-ionosphere-thermosphere system and the effects of the neutral wind on the system.

4.2. Energy Transfer

[40] We have investigated the energy transfer in the magnetosphere-ionosphere-thermosphere system using a method described by *Cowley et al.* [2005]. The power per unit area extracted from the planetary rotation into the magnetosphere-ionosphere coupling system is given by

$$P = \Omega_J \tau = \Omega_J r_i J_i B_i, \tag{21}$$

where τ is the torque per unit area of the ionosphere associated with the $\vec{J} \times \vec{B}$ force. Other notations are the same as those in section 2. The power per unit area used for the magnetospheric plasma acceleration is

$$P_M = \omega\tau = \omega r_i J_i B_i. \tag{22}$$

The remainder of the extracted energy is consumed in the upper atmosphere,

$$P_A = (\Omega_J - \omega)\tau = (\Omega_J - \omega) r_i J_i B_i. \tag{23}$$

This power consists of two components: Joule heating, P_J, and the ion drag power associated with subcorotation of the neutral atmosphere against the planetary rotation, P_D, described as follows,

$$P_J = (v_n/r_i - \omega)\tau = (v_n/r_i - \omega) r_i J_i B_i, \tag{24}$$

$$P_D = (\Omega_J - v_n/r_i)\tau = (\Omega_J - v_n/r_i) r_i J_i B_i. \tag{25}$$

As seen in equations (24) and (25), the neutral velocity determines the division between energy consumption in the upper atmosphere due to Joule heating and that due to ion-drag acceleration [*Smith et al.*, 2005].

[41] Figure 5 shows the latitudinal distribution of powers defined by equations (21)–(25). P_M and P_J dominate in the latitude regions lower and higher than 73.5°, respectively. This relation between P_M and P_J depends upon the magnetospheric plasma angular velocity ω, which decreases with increasing radial distance. When we move from lower to higher latitudes, $P_A \equiv P_J + P_D$ becomes larger than P_M at the region, between 73.5° and 74°, where ω is less than 0.5 Ω_J. The integrated values of P_M, P_J, and P_D over a hemisphere are found to be 6.4×10^{13} W, 3.2×10^{13} W, and 7.9×10^{11} W, respectively. The integrated value for the Joule heating is consistent with the estimated value of 2×10^{13}–10^{14} W based on observations [*Bhardwaj and Gladstone*, 2000].

4.3. Effect of Neutral Dynamics on the Coupling System

4.3.1. Estimation Method

[42] We now describe the effects of the neutral dynamics on the coupling system, using parameters presented and summarized by *Millward et al.* [2005]. The electric field imposed on the ionosphere originating from magnetospheric plasma convection in the planetary rotation frame is described as

$$|E_J| = B_i r_i (\Omega_J - \omega), \tag{26}$$

while the field in the neutral frame is

$$|E_n| = B_i (u_n - r_i\omega), \tag{27}$$

where u_n is the neutral velocity in the rest frame. The reduction of the electric field due to neutral dynamics is then defined as follows

$$\frac{E_n}{E_J} = 1 - \frac{(\Omega_J - u_n/r_i)}{(\Omega_J - \omega)} \equiv 1 - k. \tag{28}$$

Note that k is a function of altitude and latitude. The coupling parameter $K \equiv (\Omega_J - \Omega_n)/(\Omega_J - \omega)$, where $\Omega_n = u_n/r_i$, is used in the coupling current models [e.g., *Cowley and Bunce*, 2001]. K is related to k through the following relation

$$K \equiv 1 - \frac{\int_z \sigma_P (1-k) dz}{\int_z \sigma_P dz} = \frac{\int_z \sigma_P k\, dz}{\int_z \sigma_P dz}, \tag{29}$$

where σ_P is the Pedersen conductivity. Integrations are taken over the whole altitude region of our model. If the neutral atmosphere is rigidly corotating ($u_n/r_i = \Omega_J$), k is zero. On the other hand, if the neutral angular velocity becomes the same as the angular velocity of the magnetospheric plasma ($u_n/r_i \sim \omega$), k becomes 1. Since the neutral dynamics at auroral latitudes is largely controlled by the ion drag, k and K are generally indicative of effects of neutral-ion coupling. The neutral dynamics, however, are also affected by other effects, such as the Coriolis force and viscosity. These acceleration terms increase the neutral velocity to values larger than that caused by the ion drag alone, which corresponds to $k > 1$. In the case of the westward neutral wind, as seen in this study, k is less than 1 and E_n points equatorward when the neutral wind angular velocity exceeds that of the magnetospheric plasma (in the rest frame). On the other hand, k is larger than 1 and E_n points poleward when the angular velocity of the neutral wind is smaller than that of the magnetospheric plasma.

[43] In addition, K is related to the reduction parameter α, defined by *Huang and Hill* [1989] as,

$$\alpha \equiv \frac{1}{\Sigma}\int_z \sigma_P(z)\left(1-\frac{\Omega_J - u_n/r_i}{\Omega_J - \omega}\right)dz = \frac{1}{\Sigma}\int_z \sigma_P(z)\,(1-k(z))\,dz = 1-K. \quad (30)$$

4.3.2. Effect of Neutral Dynamics

[44] Figure 6a shows the distribution of k in the meridional plane of the polar region at 60°–75° latitudes. The values of k increase with increasing altitude, and also increase with decreasing latitude, becoming greater than 1. The increasing values of k at higher altitudes result from the thin atmosphere, where the neutral wind is easily accelerated. The increasing values of k in the lower latitude region are due to the motion of the magnetospheric plasma which almost corotates with the planet in the inner magnetosphere (see Figure 2a). In addition to the ion drag, wind acceleration in the auroral region, especially due to the Coriolis force (Figures 3b and 4), results in values $k > 1$.

[45] Figures 6b and 6c show latitude profiles of the FAC density and K, respectively. The value of K (solid line in Figure 6c) mostly increases with decreasing latitude in the latitude region below 74° from the value 0.22 at 73° where the FAC maximum appears. We separate the value of K in the regions with $k < 1$ from that in the region with $k > 1$, because E_n and the Pedersen current is directed equatorward when $k < 1$, while E_n is directed poleward when $k > 1$ as described above. $K(k < 1)$ (dashed line in Figure 6c) is almost constant with the value of 0.25 ~0.35 in the region between 73° and 66°.

[46] In order to understand contributions of neutral wind to the coupling system, we replace K, defined by equation (29), with K' as a function of z as follows,

$$K'(z) \equiv 1 - \frac{\int_{Z_1}^{Z}\sigma_P(1-k)\,dz}{\int_{Z_1}^{Z}\sigma_P\,dz}, \quad (31)$$

where z_1 is the altitude at the lower boundary. From this definition, K' increases with altitude z and corresponds to K at the top of the thermosphere. The altitude where $K' \sim 0.9\,K$ is plotted by diamonds in Figure 6a. Figure 6 shows that the neutral dynamics at altitudes below 550 km yield $K' \sim 0.9\,K$ around the main oval. Although the neutral wind velocity is larger at higher altitudes, the conductivity profile with a local maximum value at ~250 km confines the effects of the neutral dynamics on the current system to the lower-altitude region.

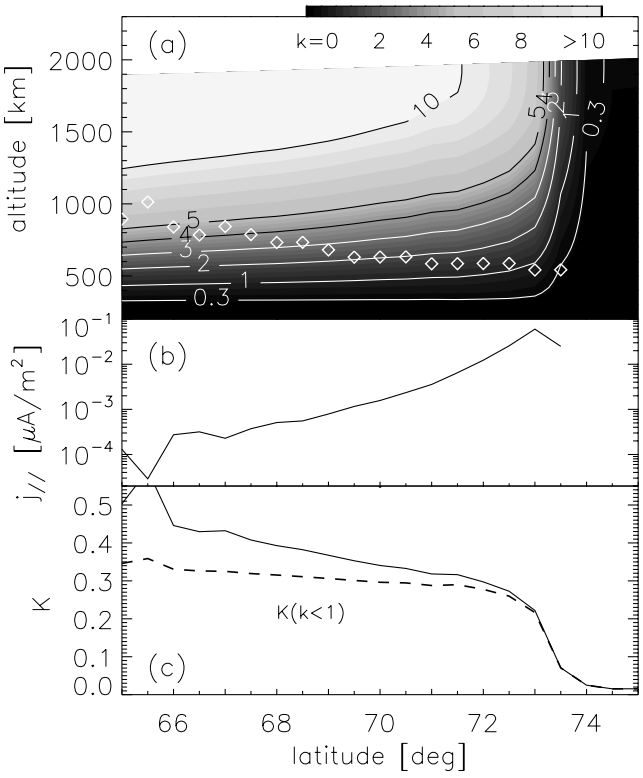

Figure 6. (a) Altitude and latitude distribution of the index k obtained from the model calculation, together with (b) latitude distributions of the FAC density and (c) latitude distributions of K. Below the altitudes shown by the white diamonds in Figure 6a, the neutral dynamics contributes to determination of ~90% of K. In Figure 6c, the solid and dashed lines are the values of k integrated in the regions over all altitudes and the $k < 1$ region, respectively.

4.3.3. Comparison With Previous Studies

[47] We have compared our results with those estimated in previous studies by *Huang and Hill* [1989] and *Millward et al.* [2005]. Coupling current models [e.g., *Nichols and Cowley*, 2004] used the value of $K = 0.5$. *Huang and Hill* [1989] obtained the altitude profile of $k(z)$ from two equations: the equation of momentum balance between ion-neutral collisions and the $\vec{J} \times \vec{B}$ force for the ionospheric ions, and the equation of momentum balance between the ion-neutral collision force and the vertical eddy-diffusion viscosity force for the neutrals, assuming that both the ions and neutrals corotate at the ionospheric lower boundary. The calculated values of $k(z)$ increase with increasing altitude. Our result, shown in Figure 6a, is similar to the profile given by *Huang and Hill* [1989] while the absolute value is different. The value of k sometimes exceeds 1 in our result, while their result shows $k \leq 1$. This difference, $k > 1$ or $k < 1$, is caused by the effects of the

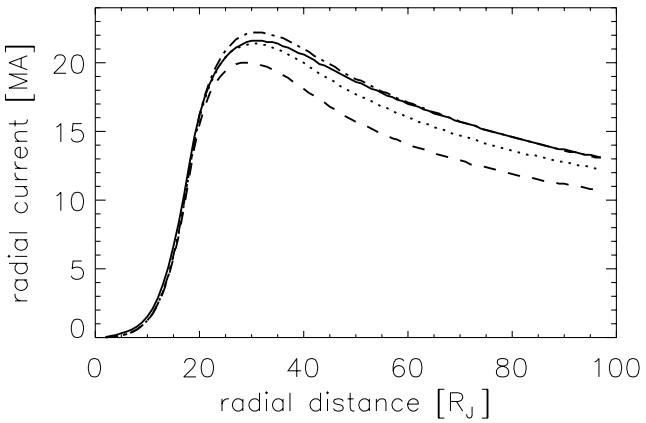

Figure 7. Radial profiles of the azimuthally integrated radial current depending on K values. The solid line is the result from the initial model setting (same as Figure 2b), while those using fixed values of K = 0.05, 0.15, and 0.25 are shown by dot-dashed, dotted, and dashed lines, respectively.

Coriolis force and horizontal viscosity on the neutral dynamics in our model as discussed in section 4.3.1. In qualitatively, they estimated $K \equiv 1 - \alpha = 99–20\%$ for a reasonable range of the eddy diffusion coefficient (10^{12}–10^{15} $n^{1/2}$ $m^{1/2}$/s, where n is the neutral number density), and K approaches to 0 when the coefficient increases to 10^{16} $n^{1/2}$ $m^{1/2}$/s. Our estimated value, $K \sim 22\%$, is well within but small part of their estimated value. We would like to raise the following two possible reasons for the smallness of our result. One is our small FAC which is close to the lower boundary of the observed FAC range [*Gustin et al.*, 2004a], because K would increase with increasing FAC as shown by *Millward et al.* [2005]. The other one would be the effect of the molecular viscosity. Since *Huang and Hill* [1989] showed that $K \equiv 1 - \alpha$ decreases with increasing the vertical diffusion coefficient, the additional molecular diffusion effect would also decrease K in this region.

[48] Using JIM, *Millward et al.* [2005] derived the altitude profile of k and its dependence on the electron energy flux and electric field imposed on the auroral region. The $k(z)$ profile derived by *Millward et al.* [2005] showed a local maximum at the peak altitude of the electron density. The large electron density contributed to enhancements of the ion drag force which accelerated the neutral wind in the anticorotation direction. There are two possible reasons for the discrepancy between the k profiles in our model and JIM. One is the auroral electron energy, since JIM used a monoenergetic auroral electron flux while we assume a broad distribution. If a broad energy spectrum is applied, the altitude distribution of k is smoothed. The other is the integration time for the model calculations. The JIM calculation interval of ~11 hours seems to be insufficient to reach a quasi steady state because the vertical transport of angular momentum by molecular viscosity (timescale ~27 hours) and by vertical convection (~1000 hours at 400 km altitude) have longer timescales than their simulation time. We therefore performed model calculations for ~2000 hours. During this long integration interval, viscosity transfers the angular momentum and smoothes its distribution over a wide altitude range. The profile of the zonal wind from our model is similar to that obtained by JTGCM [*Bougher et al.*, 2005], which also uses a long integration time.

[49] The absolute value of k in the main oval for JIM, <0.2–0.8, is smaller than 1 [*Millward et al.*, 2005]. The absence of $k > 1$ region in JIM would be also affected by the auroral spectrum and the shorter calculation period through the viscosity effect mentioned above. In addition, whether a particular position is in the main oval or in the lower latitude region is also important. *Millward et al.* [2005] showed that K at a point in the main oval is proportional to the assumed auroral flux in JIM, while our results show a value of K which is almost independent of the spatially varying FAC. The spatial variation in our model includes not only the flux variation, as in JIM, but also the spatial variations of the magnetic and electric fields and the position relative to the main oval. The independence of $K(k < 1)$ on the FAC in our model would be caused by the relative importance of the effects of spatially variable magnetic and electric fields.

4.3.4. Effect of Spatial Distribution of K on Radial Current Profile

[50] Previous coupling models have assumed a uniform and constant value of K. Here we examine the dependence of the spatial variation of K on the current distribution in the following manner. In this case, the Pedersen current is described by equation (32) instead of equation (11) with a spatially constant K,

$$J_i = \int_z \sigma_P E_n dz \approx \Sigma B_i r_i (\Omega_J - \omega)(1 - K). \qquad (32)$$

Note that the neutral wind velocity is not considered in the Pedersen current estimation although we calculate thermospheric dynamics as in section 2.1.

[51] Figure 7 shows the radial profiles of the radial current calculated with K = 0.05 (dot-dashed line), 0.15 (dotted line), and 0.25 (dashed line). The calculated value with the spatially variable K (original calculation) is also shown in Figure 7 (solid line) as a reference. The larger the assumed constant K is, the smaller the radial current that flows. The maximum current reaches 20.0 MA for K = 0.25, 21.4 MA for K = 0.15, and 22.2 MA for K = 0.05.

[52] A larger K with a smaller radial current has a smaller $\vec{J} \times \vec{B}$ force to maintain rotation of the magnetospheric plasma, and drives larger anticorotational neutral winds. As a result, K would decrease. In the opposite case, smaller K with larger current accelerates the magnetospheric plasma thus decreasing the corotation lag, such that the lag of the neutral wind will decrease, thus increasing K. From this negative feedback effect of K on the current, equilibrium for K is achieved using a self-consistent treatment. The radial current within 15 R_J in the variable K case is almost identical with those in the constant K cases. The radial profile of the current in 15–40 R_J (>50 R_J) becomes parallel (unparallel) to those in the constant K cases. This reflects the shift of K from almost constant values of ~0.3 at latitudes 70°–72.5° to smaller values at higher latitudes, as seen in Figure 6c.

4.4. Sensitivity of the Radial Current

[53] *Nichols and Cowley* [2004] were the first to compare a radial profile of the radial current obtained from the

coupling current model with that estimated from the magnetic field observations [*Khurana*, 2001]. The latter is plotted with crosses in Figure 8. The absolute value of the current reaches 80–100 MA at radial distances above 25 R_J. On the other hand, our estimated current, ~20 MA, is smaller than observed values. This is consistent with the smaller electron densities at the auroral peak compared to observations, as mentioned in section 4.1. In this section, we checked the following five possible reasons for the small current within the model: the auroral energy spectrum, the effect of the field-aligned voltage on scattered electrons, the magnetospheric magnetic field structure, the background ionospheric conductance, and the radial current at outer boundary.

[54] The energy spectrum of the precipitating electrons is one of the most ambiguous parameters in modeling studies because of the lack of direct observations. EUV auroral observations suggest that the precipitating electrons typically have high characteristic energies of 50–150 keV [*Gustin et al.*, 2004a]. We have thus also calculated the radial current with the fixed energy spectrum obtained from EUV spectral observations by *Gustin et al.* [2004b]. This spectrum consists of six Maxwellian components with peaks at 1, 4, 9, 25, 40, and 100 keV as follows,

$$\Phi_{\text{aurora}}(E) = \sum_{i=1,2,\ldots,6} c_i \phi_i \frac{E}{E_i} \exp\left(-\frac{E}{E_i}\right), \tag{33}$$

where c_1, c_2, ..., c_6 are normalization constants; φ_1 = 0.010 W/m^2, E_1 = 100 keV; φ_2 = 0.10 W/m^2, E_2 = 40 keV; φ_3 = 0.080 W/m^2, E_3 = 25 keV; φ_4 = 0.008 W/m^2, E_4 = 9 keV; φ_5 = 0.030 W/m^2, E_5 = 4 keV; φ_6 = 0.050 W/m^2, E_6 = 1 keV. The radial current obtained in this case takes a maximum value of 10 MA, as shown by the dotted line in Figure 8, which is almost a half of the profile obtained in the initial model setting shown by the solid line. The spectrum described by equation (33) has a wide electron energy range containing not only high energy electrons that enhance ionospheric conductivity, but also a large flux of low energy components which heat the upper thermosphere. Therefore the relatively small flux of high-energy electrons for the same current density causes the smaller conductance [see *Hiraki and Tao*, 2008].

[55] Precipitating auroral electrons are scattered in the atmosphere. Part of the electron energy is deposited in the atmosphere through collision processes, while the remainder returns to the out of the atmosphere [e.g., *Waite et al.*, 1983]. The escaping electrons carry a downward-directed current, which is not considered in our model. On the other hand, previous studies [e.g., *Cowley and Bunce*, 2001] have suggested the existence of a field-aligned voltage. The observed electron energy (> several tens keV) and FAC density ~0.04–0.4 μA/m^2 as indicated previously are both larger than those estimated from the electrons observed in the magnetospheric equator without an acceleration voltage (2.5 keV and 0.0134 μA/m^2, respectively). Based on the Knight relation [*Knight*, 1973; *Nichols and Cowley*, 2004], the voltage would be several tens of kilovolts. This then determines the energy of the primary energy of electrons. This voltage reflects the escaping electrons and returns them to the atmosphere. Assuming little temporal and spatial variations of the electric field, the reflected electrons obtain the same energy as their escaping energy. Using the parameterization equations which include the return of the escaping electrons (see Appendix A2) instead of the original parameterization equations, we obtain the radial current distribution for this case. The dot-dashed line in Figure 8 shows that in this case there is several MA increase in current above 30 R_J, with a maximum value of 25 MA at 32 R_J.

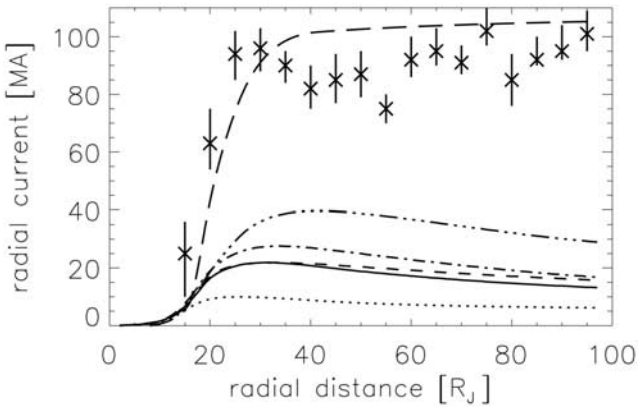

Figure 8. Radial profiles of the azimuthally integrated radial current at the magnetospheric equator contributed from both hemispheres. The solid line shows the profile obtained in the initial model setting (as in Figure 2b). The crosses indicate the radial current estimated from the magnetic field observations by *Khurana* [2001] and *Nichols and Cowley* [2004, Figure 15b]. The short-dotted line shows the result calculated using the electron energy spectrum by *Gustin et al.* [2004b]. The dot-dashed line is the result including the reflection effect of the field-aligned voltage. The short-dashed line is obtained from the different magnetospheric field structure. The triple-dot-dashed line shows the result from the case with enhanced solar EUV flux. The long-dashed line denotes the result from the case with the fixed radial current at the outer boundary of the model.

[56] *Cowley et al.* [2002] suggested that the magnetic field structure affects the current system through the mapping of the magnetospheric region on the ionosphere. The field structure is variable, e.g., depending on the local time [*Kivelson and Khurana*, 2002] and magnetospheric condition [e.g., *Woch et al.*, 1998]. For a sensitivity test on the field structure, we replaced the value of the spatial gradient 2.71 with 2.81 in equations (19) and (20) to obtain a more stretched current sheet condition. The value of 2.81 is well within the observed profile [*Kivelson and Khurana*, 2002]. The radial current increases by 0–5 MA in the radial distance above 40 R_J, as shown by the short-dashed line in Figure 8. This magnetic field dependence is caused by the following two effects. One is the concentration of the magnetic flux tubes in the ionosphere, which increases the FAC density. The other is that the smaller magnetic field at the magnetospheric equator results in a larger subcorotation of the magnetospheric plasma through the reduction of the $\vec{J} \times \vec{B}$ force, which increases the electric field as well as the current.

[57] In addition, we investigate the effect of the background conductance in the ionosphere on the radial current distribution. The solar flux model has a large ambiguity at shorter wavelengths, which strongly affects the conductance

in the low altitude region. In addition, *Kim et al.* [2001] estimated the ion population produced by meteoroid ablation to explain the observed electron enhancement at low altitudes of ~400 km. They found that this process would increase the ion density by two orders of magnitude. Since we have little information on the ionization sources which cause these ambiguities, here we only check the sensitivity of our results on the conductance, depending on an enhanced solar EUV flux. We performed a simulation using the solar EUV flux at the subsolar point (χ = 0 at the equator) instead of the longitudinally averaged one. The triple-dot-dashed line in Figure 8 shows the result in this case. The radial current has a peak value of 40 MA at 39 R_J. The result of the sensitivity check thus indicates that the background conductance has a significant effect on the resulting radial current.

[58] *Nichols and Cowley* [2004] assumed the value of the radial current (100 MA) at the outer boundary (100 R_J) of their model based on observation. The outer boundary condition of the large radial current imposes the large current on the coupling current system. On the other hand, our model does not include such a current driver or external force, which would be one of causes for the small current. We check the effects of the radial current driven at the outer boundary on the coupling current system as follows. We assume the current J_i at colatitude θ = 15–16°, which corresponds with the radial current of 100 MA at the magnetospheric outer boundary. For this case, the radial current becomes ~100 MA above 35 R_J as shown by the long-dashed line in Figure 8. The maximum FAC density takes 0.29 μA/m^2 at 20 R_J and 73° latitude, which is also in agreement with observations. The detailed description in this case and comparison between our results and studies of other coupling current models will be shown in a future work.

[59] Since the calculated radial current without the assumption for the radial current at the outer boundary of the model is smaller than the observed ones, there may be additional processes and/or ambiguities in the estimation of the FAC and/or ionospheric conductance. Here we note that the distributions of the current, thermospheric temperature, and wind patterns calculated above (in the first four cases in this sensitivity test) are similar to those seen in sections 3.1 and 3.2, which indicates that the contribution of the neutral dynamics to the current system discussed in section 4.3 is independent of the radial current at the outer boundary. On the other hand, the radial current in addition to the closed current system would also be a key for the observed current structure of *Khurana* [2001] shown by *Nichols and Cowley* [2004] as well as spatial and temporal variations of observed aurora. In this case, a source of the current beyond our model treatment would be a new interesting question. The future planning improvement of the magnetospheric part of our model, i.e., including the magnetohydrodynamic (MHD) effect, will enable us to describe the current more quantitatively. In addition, more observations of the ionospheric parameters and the currents are essential to model physical processes accurately and to understand the current system.

5. Summary and Conclusions

[60] In order to understand the coupling processes between the Jovian magnetosphere, ionosphere, and thermosphere, we have developed an axisymmetric model which simultaneously calculates the two-dimensional thermospheric dynamics, the magnetospheric plasma convection, and the coupling current between the magnetosphere and ionosphere. Using this newly developed model, we have investigated energetic transfer in the coupled system and the effects of the neutral dynamics on the current. The main results from this study are summarized as follows.

[61] 1. The model, which has a high spatial resolution at auroral latitudes (0.5°), represents well the zonally averaged characteristics of the meridional thermospheric temperature and wind estimated from JTGCM, that is high temperatures in the polar region and a neutral circulation from the auroral region to lower latitudes. The anticorotating zonal wind is formed both by Coriolis forces and ion drag. Our model provides a self-consistent and physically appropriate treatment of the neutral dynamics, the ionospheric conductance, the FAC, and the electric field. Some values, i.e., temperature, neutral wind dynamics, ion wind velocity, and FAC density are consistent with observations, while the obtained ion densities are smaller than observations.

[62] 2. The energy extracted from planetary rotation in the magnetosphere-ionosphere coupling system is used mainly for magnetospheric plasma acceleration in the region below 73.5° latitude, while above 73.5° latitude the energy is consumed in the upper atmosphere mainly through Joule heating. The neutral wind velocity is an important parameter for determining the partition of the energy consumption in the upper atmosphere, i.e., Joule heating or ion-drag acceleration. Our calculation shows that the former is an order of magnitude higher than the latter. The integrated input power over one hemisphere, $\sim 1 \times 10^{14}$ W, is consistent with estimated values based on auroral observations.

[63] 3. The neutral wind dynamics contributes to a reduction of the electric field by ~22% compared to the case of rigid neutral corotation in the main oval region. About 90% of this reduction is attributable to neutral winds below 550 km altitude. The reduction parameter k estimated in our model varies spatially. The value of k increases not only with increasing altitude as suggested by previous studies, but also with decreasing latitude in the auroral region between 66° and 74°. We have found a region of $k > 1$ where the neutral wind velocity is larger than the ion drift velocity in the planetary rotation frame caused by Coriolis forces and viscosity. The effect of the spatial variation of K is seen especially in large radial distances which correspond to the poleward region of the main oval.

[64] 4. The current in the magnetosphere-ionosphere coupling circuit estimated in our model is smaller than those determined from observations by a factor of ~4. We have checked the sensitivity of the radial current to the following effects. The radial current estimated using a fixed electron energy spectrum is almost a half of those obtained in the initial spectrum variable model setting. The magnetic field and return of the escaping electrons due to a field-aligned voltage increase the radial current by less than 10 MA. Enhancement of the background ionospheric conductance, e.g., enhancement of the solar EUV, can produce the radial current of 40 MA in the region at 39 R_J. If we assume the radial current of 100 MA at the outer boundary of the model, the current shows a large value comparable with observations.

[65] The background ionospheric conductance and/or the radial current at large radial distance are candidates for

maintaining the observed current distributions and their variations. The detailed comparison between results obtained from coupling models with different assumptions and approaches would bring more insights into the current system. In addition, the future improvement of the magnetospheric part of our model, i.e., including the MHD model, will enable us to describe the current more quantitatively.

Appendix A: Parameterized Equation for Ionization Rate by Auroral Electron

A1. Basic Equations

[66] *Hiraki and Tao* [2008] provided equations representing the ionization rate of a H_2 atmosphere due to precipitating auroral electrons. They performed Monte Carlo simulations to obtain the ionization rate and the results were parameterized based on the formulation for the terrestrial atmosphere by *Rees* [1963].

[67] The ionization per unit volume $Q_{\mathrm{ion}}(\varepsilon_0, z)$ (/m^3) for a flux $\Phi_{\mathrm{aurora}}(\varepsilon_0)$ (/m^{2}s) at an initial energy ε_0 (keV) is given by

$$\frac{Q_{\mathrm{ion}}(\varepsilon_0, z)}{\Phi_{\mathrm{aurora}}(\varepsilon_0)} = \frac{\varepsilon_0}{\varepsilon_{\mathrm{ion}}} \frac{\lambda(\varepsilon_0, R/R_0(z))}{R_0(z)} \rho(z), \tag{A1}$$

where $\varepsilon_{\mathrm{ion}}$ (keV) is the energy loss per ionization, taken as 0.030 keV; $\rho(z)$ is the atmospheric density in units of kg/m^3 at altitude z; R and R_0 are respectively the atmospheric depth in kg/m^2 at the altitude of interest and at the maximum range of the incident electrons; λ is the normalized energy distribution function. R_0 and λ are represented as a function of $x = R/R_0$ as follows,

$$R_0 = 3.39 \times 10^{-5} \varepsilon_0^{1.39}, \tag{A2}$$

$$\lambda(\varepsilon_0, R/R_0) = k(\varepsilon_0) \lambda_0(R/R_0), \tag{A3}$$

$$k(\varepsilon_0) = 0.13 + 0.89(1 - 1.1 \tanh(\log_{10} \varepsilon_0 - 1)), \tag{A4}$$

$$\lambda_0(x) = \begin{cases} -669.53x^4 + 536.18x^3 - 159.86x^2 + 18.586x + 0.5064 & 0 \le x \le 0.3 \\ 0.767x^4 - 5.9034x^3 + 12.119x^2 - 9.734x + 2.7470 & 0.3 < x \le 0.825 \\ -0.8091x^3 + 2.4516x^2 - 2.4777x + 0.8353 & 0.825 < x \le 1 \end{cases}. \tag{A5}$$

We obtain the ionization rate using these equations with arbitrary H_2 density $\rho(z)$ and an auroral electron flux $\Phi_{\mathrm{aurora}}(\varepsilon_0)$.

A2. Parameterized Equations Including Electron Return Effects

[68] Precipitating auroral electrons are scattered in the atmosphere. Part of the electron energy is deposited into the atmosphere through collision processes, while the remainder returns to the magnetosphere. When a significant field-aligned voltage is present, the scattered electrons will be reflected and return into the atmosphere.

[69] We modify the parameterized formulas in Appendix A1 to include the effect of returning escape electrons based on the ionization rate obtained from modified Monte Carlo simulations. In addition to the original simulation setting, we reenter the scattered electrons (note that the scattered electrons are not assumed but are calculated in the simulation) into the atmosphere with the same energy as their escaping energy. In this setting, we assume a steady field-aligned voltage and little spatial variation of the field compared to horizontal transition of electrons. The parameterized formulas in this case are as follows.

$$R_0 = 3.31 \times 10^{-5} \varepsilon_0^{1.41}, \tag{A6}$$

$$k(\varepsilon_0) = 0.56 + 0.37(1 - 1.2 \tanh(0.8 \log_{10} \varepsilon_0 - 0.98)), \tag{A7}$$

$$\lambda_0(x) = \begin{cases} -578.9x^2 + 45.16x + 1.271 & 0 \le x \le 0.04 \\ -780.2x^6 + 1876.x^5 - 1819.x^4 + 904.4x^3 - 234.5x^2 + 23.04x + 1.613 & 0.04 < x \le 0.6 \\ -5.868x^3 + 15.12x^2 - 13.12x + 3.851 & 0.6 < x \le 1 \end{cases}. \tag{A8}$$

We obtain the ionization rate including electron return effects using equations (A1), (A3), and (A6)–(A8) with arbitrary H_2 density $\rho(z)$ and an auroral electron flux $\Phi_{\mathrm{aurora}}(\varepsilon_0)$.

[70] **Acknowledgments.** C. Tao thanks Dr. Y. Hiraki, Prof. S. W. H. Cowley, and Dr. J. D. Nichols for useful discussions. This work is supported by a research fellowship from the Japan Society for the Promotion of Science (JSPS) and by the 21st Century COE program of the JSPS "Advanced science and technology center for the dynamics Earth" and the Global COE program "Global education and research center for Earth and planetary dynamics" at Tohoku University. We thank the referees for their productive and valuable comments.

[71] Wolfgang Baumjohann thanks Stanley Cowley and Nicholas Achilleos for their assistance in evaluating this paper.

References

Achilleos, N., S. Miller, J. Tennyson, A. D. Aylward, I. Mueller-Wodarg, and D. Rees (1998), JIM: A time-dependent, three-dimensional model of Jupiter's thermosphere and ionosphere, *J. Geophys. Res.*, *103*(E9), 20,089–20,112.

Barbosa, D. D., D. A. Gurnett, W. S. Kurth, and F. L. Scarf (1979), Structure and properties of Jupiter's magnetoplasmadisc, *Geophys. Res. Lett.*, *6*(10), 785–788.

Bhardwaj, A., and G. R. Gladstone (2000), Auroral emissions of the giant planets, *Rev. Geophys.*, *38*(3), 295–353.

Bougher, S. W., J. H. Waite Jr., T. Majeed, and G. R. Gladstone (2005), Jupiter Thermospheric General Circulation Model (JTGCM): Global structure and dynamics driven by auroral and Joule heating, *J. Geophys. Res.*, *110*, E04008, doi:10.1029/2003JE002230.

Chapman, S., and T. G. Cowling (1970), *The Mathematical Theory of Non-Uniform Gases*, pp. 86–87, Cambridge Univ. Press, Cambridge, U. K.

Clarke, J. T., D. Grodent, S. Cowley, E. Bunce, P. Zarka, J. Connerney, and T. Satoh (2004), Jupiter's aurora, in *Jupiter: The Planet, Satellites and Magnetosphere*, edited by F. Bagenal, B. McKinnon, and T. Dowling, pp. 639–670, Cambridge Univ. Press, Cambridge, U. K.

Cowley, S. W. H., and E. J. Bunce (2001), Origin of the main auroral oval in Jupiter's coupled magnetosphere-ionosphere system, *Planet. Space Sci.*, *49*, 1067–1088.

Cowley, S. W. H., and E. J. Bunce (2003), Modulation of Jupiter's main auroral oval emissions by solar wind induced expansions and compressions of the magnetosphere, *Planet. Space Sci.*, *51*, 57–79.

Cowley, S. W. H., J. D. Nichols, and E. J. Bunce (2002), Distributions of current and auroral precipitation in Jupiter's middle magnetosphere computed from steady-state Hill-Pontius angular velocity profiles: Solutions for current sheet and dipole magnetic field models, *Planet. Space Sci.*, *50*, 717–734.

Cowley, S. W. H., I. I. Alexeev, E. S. Belenkaya, E. J. Bunce, C. E. Cottis, V. V. Kalegaev, J. D. Nichols, R. Prangé, and F. J. Wilson (2005), A simple axisymmetric model of magnetosphere-ionosphere coupling currents in Jupiter's polar ionosphere, *J. Geophys. Res.*, *110*, A11209, doi:10.1029/2005JA011237.

Cowley, S. W. H., J. D. Nichols, and D. J. Andrews (2007), Modulation of Jupiter's plasma flow, polar currents, and auroral precipitation by solar wind-induced compressions and expansions of the magnetosphere: A simple theoretical model, *Ann. Geophys.*, *25*, 1433–1463.

Danby, G., B. K. Elza, M. A. Morrison, and W. K. Trail (1996), The separable representation of exchange in electron-molecule scattering: I. Elastic scattering and rotational excitation, *J. Phys. B.: At., Mol. Opt. Phys.*, *29*, 2265–2287.

Durran, D. R. (1999), *Numerical Methods for Wave Equations in Geophysical Fluid Dynamics*, Springer, New York.

Grodent, D., J. H. Waite Jr., and J.-C. Gérard (2001), A self-consistent model of the Jovian auroral thermal structure, *J. Geophys. Res.*, *106*(A7), 12,933–12,952.

Gustin, J., J.-C. Gérard, D. Grodent, S. W. H. Cowley, J. T. Clarke, and A. Grard (2004a), Energy-flux relationship in the FUV Jovian aurora deduced from HST-STIS spectral observations, *J. Geophys. Res.*, *109*, A10205, doi:10.1029/2003JA010365.

Gustin, J., et al. (2004b), Jovian auroral spectroscopy with FUSE: Analysis of self-absorption and implications for electron precipitation, *Icarus*, *171*, 336–355.

Hill, T. W. (1979), Inertial limit on corotation, *J. Geophys. Res.*, *84*(A11), 6554–6558.

Hill, T. W. (1980), Corotation lag in Jupiter's magnetosphere: Comparison of observation and theory, *Science*, *207*, 301–302.

Hill, T. W. (2001), The Jovian auroral oval, *J. Geophys. Res.*, *106*(A5), 8101–8107.

Hiraki, Y., and C. Tao (2008), Parameterization of ionization rate by auroral electron precipitation in Jupiter, *Ann. Geophys.*, *26*, 77–86.

Huang, T. S., and T. W. Hill (1989), Corotation lag of the Jovian atmosphere, ionosphere, and magnetosphere, *J. Geophys. Res.*, *94*(A4), 3761–3765.

Khurana, K. K. (2001), Influence of solar wind on Jupiter's magnetosphere deduced from currents in the equatorial plane, *J. Geophys. Res.*, *106*(A11), 25,999–26,016.

Knight, S. (1973), Parallel electric fields, *Planet. Space Sci.*, *21*, 741–750.

Kim, Y. H., and J. L. Fox (1994), The chemistry of hydrocarbon ions in the Jovian ionosphere, *Icarus*, *112*, 310–325.

Kim, Y. H., W. Dean Pesnell, J. M. Grebowsky, and J. L. Fox (2001), Meteoric ions in the ionosphere of Jupiter, *Icarus*, *150*, 261–278.

Kivelson, M. G., and K. K. Khurana (2002), Properties of the magnetic field in the Jovian magnetotail, *J. Geophys. Res.*, *107*(A8), 1196, doi:10.1029/2001JA000249.

Lystrup, M. B., S. Miller, N. D. Russo, R. J. Vervack Jr., and T. Stallard (2008), First vertical ion density profile in Jupiter's auroral atmosphere: Direct observations using the KECK II telescope, *Astrophys. J.*, *677*, 790–797.

Majeed, T., J. H. Waite Jr., S. W. Bougher, and G. R. Gladstone (2005), Processes of equatorial thermal structure at Jupiter: An analysis of the Galileo temperature profile with a three-dimensional model, *J. Geophys. Res.*, *110*, E12007, doi:10.1029/2004JE002351.

Matcheva, K. I., and D. F. Strobel (1999), Heating of Jupiter's thermosphere by dissipation of gravity waves due to molecular viscosity and heat conduction, *Icarus*, *140*, 328–340.

McNutt, R. L., Jr., J. W. Belcher, and H. S. Bridge (1981), Positive ion observations in the middle magnetosphere of Jupiter, *J. Geophys. Res.*, *86*(A10), 8319–8342.

Melin, H., S. Miller, T. Stallard, C. Smith, and D. Grodent (2006), Estimated energy balance in the Jovian upper atmosphere during an auroral heating event, *Icarus*, *181*, 256–265.

Millward, G., S. Miller, T. Stallard, N. Achilleos, and A. D. Aylward (2005), On the dynamics of the Jovian ionosphere and thermosphere: IV. Ion-neutral coupling, *Icarus*, *173*, 200–211.

Nichols, J. D., and S. W. H. Cowley (2004), Magnetosphere-ionosphere coupling currents in Jupiter's middle magnetosphere: Effect of precipitation-induced enhancement of the ionospheric Pedersen conductivity, *Ann. Geophys.*, *22*, 1799–1827.

Perry, J. J., Y. H. Kim, J. L. Fox, and H. S. Porter (1999), Chemistry of the Jovian Auroral Ionosphere, *J. Geophys. Res.*, *104*(E7), 16,541–16,565.

Pontius, D. H., Jr. (1997), Radial mass transport and rotational dynamics, *J. Geophys. Res.*, *102*(A4), 7137–7150.

Rees, M. H. (1963), Auroral ionization and excitation by incident energetic electrons, *Planet. Space Sci.*, *11*, 1209–1218.

Rego, D., N. Achilleos, T. Stallard, S. Miller, R. Prangé, M. Dougherty, and R. D. Joseph (1999), Supersonic winds in Jupiter's aurorae, *Nature*, *399*, 121–123.

Richards, P. G., J. A. Fennelly, and D. G. Torr (1994), EUVAC: A solar EUV flux model for aeronomic calculations, *J. Geophys. Res.*, *99*(A5), 8981–8992.

Schubert, G., M. P. Hickey, and R. L. Walterscheid (2003), Heating of Jupiter's thermosphere by the dissipation of upward propagating acoustic waves, *Icarus*, *163*, 398–413.

Schunk, R. W., and A. F. Nagy (2000), Ionization and energy exchange processes, in *Ionosphere Physics, Plasma Physics, and Chemistry*, *Cambridge Atmos. Space Sci. Ser.*, edited by J. T. Houghton, M. J. Rycroft, and A. J. Dessler, pp. 237–267 and pp. 521–531, Cambridge Univ. Press, Cambridge, U. K.

Seiff, A., D. B. Kirk, T. C. D. Knight, L. A. Young, F. S. Milos, E. Venkatapathy, J. D. Mihalov, R. C. Blanchard, R. E. Young, and G. Schubert (1997), Thermal structure of Jupiter's upper atmosphere derived from the Galileo probe, *Science*, *276*, 102–104.

Shimazaki, T. (1985), *Minor Constitudents in the Middle Atmosphere*, pp. 360–361, Terra Sci., Tokyo, Japan.

Smith, C. G. A., S. Miller, and A. D. Aylward (2005), Magnetospheric energy inputs into the upper atmosphere of the giant planets, *Ann. Geophys.*, *23*, 1943–1947.

Stallard, T. S., S. Miller, S. W. H. Cowley, and E. J. Bunce (2003), Jupiter's polar ionospheric flows: Measured intensity and velocity variations poleward of the main auroral oval, *Geophys. Res. Lett.*, *30*(5), 1221, doi:10.1029/2002GL016031.

Thomas, N., F. Bagenal, T. W. Hill, and J. K. Wilson (2004), The Io neutral clouds and plasma torus, in *Jupiter—The Planet, Satellites and Magnetosphere*, edited by F. Bagenal, T. Dowling, and W. McKinnon, pp. 561–591, Cambridge Univ. Press, Cambridge, U. K.

Tokioka, T. A. (1978), Some considerations on vertical differencing, *J. Meteorol. Soc. Jpn.*, *56*, 98–111.

Waite, J. H., Jr., T. E. Cravens, J. Kozyra, A. F. Nagy, S. K. Atreya, and R. H. Chen (1983), Electron precipitation and related aeronomy of the Jovian thermosphere and ionosphere, *J. Geophys. Res.*, *88*(A8), 6143–6163.

Waite, J. H., Jr., G. R. Gladstone, W. S. Lewis, P. Drossart, T. E. Cravens, A. N. Maurellis, B. H. Mauk, and S. Miller (1997), Equatorial X-ray emissions: Implications for Jupiter's high exospheric temperatures, *Science*, *276*, 104–108.

Woch, J., N. Krupp, A. Lagg, B. Wilken, S. Livi, and D. J. Williams (1998), Quasi-periodic modulations of the Jovian magnetotail, *Geophys. Res. Lett.*, *25*(8), 1253–1256.

Young, L. A., R. V. Yelle, R. Young, A. Seiff, and D. B. Kirk (1997), Gravity waves in Jupiter's thermosphere, *Science*, *276*, 108–111.

H. Fujiwara, Y. Kasaba, and C. Tao, Department of Geophysics, Tohoku University, 6-3, Aramaki Aoba, Aoba-ku, Sendai, Miyagi 980-8578, Japan. (tao@pat.gp.tohoku.ac.jp)